PHYSICAL REVIEW D **90,** 105030 (2014)

Anomalous magnetic moment of hot quarks, inverse magnetic catalysis, and reentrance of the chiral symmetry broken phase

Sh. Fayazbakhsh[1,*] and N. Sadooghi[2,†]

[1]*Institute for Research in Fundamental Sciences (IPM), School of Particles and Accelerators, P.O. Box 19395-5531 Tehran, Iran*

[2]*Department of Physics, Sharif University of Technology, P.O. Box 11155-9161 Tehran, Iran*

(Received 2 September 2014; published 25 November 2014)

The effect of the anomalous magnetic moment of quarks on thermodynamic properties of the chiral condensate is studied, using a two-flavor Nambu–Jona-Lasinio model at finite temperature T, chemical potential μ, and in the presence of a uniform magnetic field eB. To this purpose, the Schwinger linear-in-B ansatz for the anomalous magnetic moment of quarks is considered in terms of the nonperturbative Bohr magneton. In a two-dimensional flavor space, it leads to the correction $\hat{T}_{Sch} = \hat{\kappa}\,\hat{Q}\,eB$ in the energy dispersion relation of quarks. Here, $\hat{Q}$ is the quark charge matrix. We consider three different sets for $\hat{\kappa}$, and numerically determine the dependence of the constituent quark mass on T, μ, and eB for fixed $\hat{\kappa}$. By exploring the complete phase portrait of this model in $T-\mu$, $\mu-eB$, and $T-eB$ phase spaces for various fixed eB, T, μ, and $\hat{\kappa}$, we observe that inverse magnetic catalysis occurs for large enough $\hat{\kappa}$. Moreover, in the regime of weak magnetic fields, the phenomenon of reentrance of chiral symmetry broken and restored phases occurs for T-, μ-, and eB-dependent $\hat{\kappa}$.

DOI: 10.1103/PhysRevD.90.105030 PACS numbers: 12.38.-t, 11.30.Qc, 12.38.Aw, 12.39.-x

I. INTRODUCTION

The effects of uniform magnetic fields on relativistic quark matter have been studied extensively in recent years (for an overview, see [1]). The main interest arises from the relevance of these effects on the physics of neutron stars, as well as on the dynamics of the quark-gluon plasma created in relativistic heavy ion collisions (HICs). It is known that magnetars, a certain class of neutron stars, exhibit magnetic fields up to 10^{12}–10^{13} Gauß on their surface, and 10^{18}–10^{20} Gauß in their inner core [2]. In [3] the dynamo effect during the first few seconds after the star's gravitational collapse is made responsible for the generation of these unusual magnetic fields. Even larger magnetic fields are believed to be created in early stages of noncentral HICs. Depending on the collision energies and impact parameters of the collisions, the strength of these magnetic fields are estimated to be of the order $eB \sim 0.03$ GeV^2 at RHIC and $eB \sim 0.3$ GeV^2 at LHC [4].[1] As it is shown for the first time in [5], the magnetic fields created in noncentral HICs are time-dependent and rapidly decay after $\tau \sim 1$–2 fm/c^2.[2] However, as is described in [7], the presence of certain medium effect, like the electric conductivity, substantially delays the decay of these time-dependent magnetic fields. This is why in the most cases, the effect of constant and uniform magnetic fields on quark matter is discussed in the literature.

A uniform and spatially constant magnetic field breaks the Lorentz invariance of the physical system, and consequently induces anisotropies in the parallel and perpendicular directions with respect to the direction of the background magnetic field. The anisotropies include those in the neutrino emission and magnetic winds in the astrophysics of magnetars [3], or anisotropies arising in the refraction indices [8], and decay constants of mesons in hot and magnetized quark matter [9,10]. The latter may be relevant for the physics of heavy ion collisions. Recently, the pressure anisotropies for a gas of protons and a gas of neutrons are studied in [11]. It is, in particular, demonstrated that the inclusion of the anomalous magnetic moment (AMM) of protons and neutrons increases the level of anisotropies in both cases. Pressure anisotropies, arising from uniform and spatially fixed magnetic fields, are supposed to have significant effects on the elliptic flow v_2 in heavy ion collisions [12].

In the present paper, we apply the method used in [11], to study the effect of various T-, μ-, and eB-dependent and independent AMM of quarks on the phase diagram of a two-flavor magnetized Nambu–Jona-Lasinio (NJL) model at finite temperature T and chemical potential μ. We will explore the phenomenon of magnetic catalysis (MC),[3] and inverse magnetic catalysis (IMC),[4] as well as the reentrance of chiral symmetry broken and restored phases in the phase

*shfayazbakhsh@ipm.ir

†sadooghi@physics.sharif.ir

[1]Here, $eB = 1$ GeV^2 corresponds to $B \sim 1.7 \times 10^{20}$ Gauß.

[2]See also [6] for a recent review of this topic.

[3]The phenomenon of MC is introduced originally in [13,14], and is extensively discussed in the literature (for a recent review, see [15]).

[4]To the best of our knowledge, the term "inverse magnetic catalysis" is used for the first time in [16], but the phenomenon of IMC had been previously observed, e.g., in [17].

space of our model. The phenomenon of reentrance is already observed in the condensed matter physics of superfluidity [18] and liquid crystals [19], as well as in the astrophysics of neutron stars [20].

In our previous works [21,22], we have already studied in detail the complete $T-\mu$, $\mu-eB$, and $T-eB$ phase portraits of the magnetized two-flavor NJL model, without inclusion of the quark AMM. We mainly worked in the supercritical regime of the NJL coupling, i.e., the coupling constant of the NJL model was chosen in such a way that the system exhibited chiral symmetry breaking even for vanishing magnetic fields. In this case, the magnetic field only enhances the production of bound states; they consist of mesons in chiral symmetry broken phase (χSB) and diquarks in color symmetry broken phase. In this sense, in [22], we focused on the phenomenon of MC of chiral and color symmetry breaking, and reported about various interesting phenomena, such as de Haas-van Alphen (dHvA) oscillations [23], that lead to reentrant chiral and color symmetry broken phases, mainly in the regime of weak magnetic fields. The phenomenon of MC is discussed intensively in many contexts [15]. At zero temperature, it arises from a dimensional reduction from D to $D-2$ dimensions in the lowest Landau level (LLL). This is believed to be responsible for the aforementioned enhancement of bound state formation. As a consequence, in a massless theory, whose original Lagrangian density satisfies the chiral symmetry, a finite mass is dynamically created, which then breaks the chiral symmetry of the theory. Finite temperature and baryonic chemical potential compete with external magnetic fields in this regard, and, except in the regime of very strong magnetic fields, suppress the formation of mesonic bound states (see [22] for more details). In our model, this regime is characterized by a threshold magnetic field $eB_t \sim 0.5$ GeV^2, above which the dynamics of the fermions is solely dominated by LLL. In this regime, the constituent quark mass monotonically increases with increasing eB as a consequence of MC. In the regime $eB < 0.5$ GeV^2, however, the eB dependence of the condensate exhibits dHvA oscillations, which occur whenever Landau levels pass the quark Fermi level.[5] Thus, because of these oscillations in the regime of $eB < eB_t$, at a fixed temperature and for both vanishing and nonvanishing chemical potential, the chiral condensate exhibits two different behaviors: In some regimes, it increases with increasing eB, this is related to the phenomenon of MC. But, in some other regimes, it decreases with increasing eB. This is related to the phenomenon of IMC.

In [22], we have also studied the effect of external magnetic fields on $T-\mu$, $T-eB$, and $\mu-eB$ phase portraits of magnetized two-flavor NJL model. We have shown that, as a consequence of the background magnetic fields, second-order chiral phase transitions turn into first-order ones, and, in the regime above $eB_t \sim 0.5$ GeV^2, for fixed μ and T, the critical temperature T_c and chemical potential μ_c of χSB, monotonically increase with increasing eB. This has been supposed to be an indication of the phenomenon of MC, which is mainly a LLL dominated effect. On the other hand, it has been shown, that in the regime of weak magnetic fields, the aforementioned dHvA oscillations, lead again to two different behaviors of T_c and μ_c as a function of eB: In some regimes, T_c and μ_c increase with increasing eB, because of MC. In some other regimes, however, as a result of IMC, T_c and μ_c decrease with increasing eB. The phenomenon of reentrance of chiral (color) symmetry broken phases at certain fixed (T,μ,eB) is also believed to be a consequence of dHvA oscillations in the weak field regime [22].

Several other groups also investigate the effects of external magnetic fields on the phase diagram of hot QCD. These includes the groups working on lattice QCD at finite T, zero μ and nonvanishing eB [27–32], or investigating the QCD phase diagram by making use of functional renormalization group method [33–35]. Many other groups elaborate different QCD-like models at finite (T,μ,eB), that exhibit χSB. The latter consists of, e.g., NJL-model [36,37], Polyakov-linear-σ model [38], Polyakov-NJL model [39–41], Polyakov-Quark-Meson model [42,43], NJL model including axial chemical potential [44,45], Ginzburg-Landau model [46], charged scalar model with spontaneous χSB [47], NJL model with dynamical AMM generation [48]. Let us notice that the interest on this subject grows up after the still not fully comprehended lattice results by Bali *et al.* in [28]. They reported an unprecedented decrease of T_c as a function of eB within an ab initio lattice QCD simulation, and declared this as a signature of IMC in this framework. The physical explanation of the phenomenon of IMC is, in particular, still under investigation: In [31,40], the interaction of the magnetic field with the sea quarks leading to a backreaction of the Polyakov loop, and in [36] the magnetic inhibition because of neutral meson fluctuations are made responsible for IMC. In [45], it is explained how IMC is induced by sphalerons. Recently, in [37,41,47,48], the running of the corresponding coupling constants to the considered models, and therefore their eB dependence are taken into account, and it is shown how the lattice results on the eB dependence of T_c in [28] can be successfully reproduced.

In a parallel development, the competition between mass and eB contributions to QCD pressure is considered up to two-loop radiative corrections in [49]. It is argued that the deviation of the Landé g-factor from 2, which is of about $g-2 \sim 10^{-3}$, may produce sizable corrections to the QCD pressure. This affects the energy of the LLL by turning the mass into $m_{\rm eff}^2 = m^2 + (g-2)eB$. For the relevant $eB > 0.01$ GeV^2, the correction will be in the MeV range.

[5]De Haas-van Alphen oscillations are studied in [24,25], and recently in [26].

It may thus compete with m, and cannot be ignored in quantitative studies [49]. The effect of dynamically generated AMM of fermions on the phase diagram of a magnetized one-flavor NJL model is recently investigated in [50].[6] Here, inspired by the results presented in [53], a nonperturbative mechanism for the generation of the quark AMM is introduced. To this purpose, a one-flavor NJL Lagrangian density including an appropriate tensor channel is used. It is in particular shown, that in the subcritical regime of the NJL coupling, where the phenomenon of MC is solely responsible for χSB, two independent condensates emerge in the LLL dominant regime. They correspond to the dynamical mass and the AMM of quarks. The fact that the dynamical generation of AMM is mainly a LLL effect suggests that the Schwinger linear-in-B ansatz [54] for the quark AMM is not appropriate for massless fermions. This is argued to be in sharp contrast to theories with massive fermions, where the Schwinger ansatz is allowed in the limit of weak magnetic fields [55]. Moreover, in [50], the critical temperature of the second-order phase transition of χSB is determined in a LLL approximation, and it is shown that the generation of the quark AMM increases T_c as a function of eB, and therefore it cannot be responsible for the phenomenon of IMC. In [48], however, following the aforementioned proposal of eB-dependent coupling constant, the effect of running coupling constant of the one-flavor NJL model on T_c is studied. It is shown, that in the regime of strong magnetic fields, characterized by $eB \gg \Lambda^2_{\rm QCD}$, the coupling constant of the model becomes anisotropic, and only the coupling parallel to the direction of the background magnetic field receives contributions from quarks in a LLL approximation. Interestingly, as a result of a certain antiscreening arising from these quarks, this coupling decreases with increasing eB. The dependence of T_c on this specific coupling leads to the desired phenomenon of IMC in the strong magnetic field limit.

In the present paper, motivated by the above intriguing developments, we will consider the quark AMM in the one-loop effective potential of a magnetized two-flavor NJL model at finite T and μ. In contrast to [50–52], and similar to the method used in [11], we will induce the quark AMM by an additional term $\hat{a}\sigma_{\mu\nu}F^{\mu\nu}$ in the original Lagrangian of the model, including massive quarks. The coefficient $\hat{a}$, proportional to the Bohr magneton $\mu_B \equiv \frac{e}{2m}$, will then be identified with the quark AMM. Here, μ_B depends on the constituent quark mass $m \equiv m_0 + \sigma_0$, where m_0 is the current quark mass and σ_0 is the chiral condensate. This is in contrast to the approach described in [52], where the Bohr magneton is inversely proportional to current (bare) quark mass m_0. The aforementioned additional term $\hat{a}\sigma_{\mu\nu}F^{\mu\nu}$ in the Lagrangian density of the NJL model leads to the energy dispersion

$$E_{q_f}^{(p,s)} = \sqrt{p_3^2 + [(2p|q_f eB| + m^2)^{1/2} - sT_f]^2}, \quad (1.1)$$

for up and down quarks in the presence of a constant magnetic field. Here, $T_f = \kappa_f q_f eB$ with $\kappa_f \equiv \frac{\alpha_f}{2m}$, p labels the Landau levels, $s = \pm 1$ states for the spin of quarks, $f = u, d$ labels the up (u) and down (d) flavors, and $q_f = 2/3, -1/3$ is the charge of up and down quarks. Moreover, α_f is related to the deviation of the Landé g-factor from 2. The above additional term T_f is equivalent to the linear-in-B ansatz by Schwinger $T_f^{\rm sch} = \alpha_f q_f \mu_B B$ for T_f, with the nonperturbative (effective) Bohr magneton [53] $\mu_B = \frac{e}{2m}$. Let us notice, that in the one-loop level, α_f is proportional to the electromagnetic fine structure constant $\alpha_e = \frac{1}{137}$. Perturbatively, it receives radiative corrections from the vertex function of quarks and the background photon field. In the framework of constituent quark model [56], it appears in the ratio $I_f = \frac{M}{1+\alpha_f} = \frac{\mu_N}{\mu_f} q_f m_p$, with M the constituent (effective) quark mass,[7] $\mu_N \equiv \frac{e}{2m_p}$ the nuclear magneton, μ_f the magnetic moment of the fth quark flavor,[8] and m_p the proton mass (see Appendix or more details). As it is argued in [56], choosing the experimental values for μ_N, μ_f, q_f, and m_p, the ratio I_f is fixed to be $I_u \sim 338$ MeV for the up quark and $I_d \sim 322$ MeV for the down quark [56]. A phenomenological constant value for κ_f, compatible with the constituent quark model, can then be determined by choosing an appropriate constant value for the constituent (effective) mass M, that yields α_f, and consequently κ_f through given values of $I_f, f = u, d$, and the definition $\kappa_f = \frac{\alpha_f}{2M}$.

In this paper, we will consider three different sets for the dimensionful coupling $\kappa_f, f = u, d$ in $T_f = \kappa_f q_f eB$; two of them will be T-, μ-, and eB-independent, and arise, in the framework of constituent quark model, by separately choosing $M = 420$ MeV, and $M = 340$ MeV, and fixing α_f through the phenomenologically given ratio I_f, as described above. The third set of $\kappa_f, f = u, d$ will depend on T, μ, and eB, and include the T-dependent one-loop perturbative correction to α_f, generalized from the QED results presented in [57,58]. Plugging first (1.1) with given values of κ_f into the one-loop effective potential of our model, and then minimizing the resulting expression with respect to m, we will determine the T, μ, and eB dependence of the constituent quark mass for each fixed set of $\kappa_f, f = u, d$. The complete $T-\mu$, $\mu-eB$, and $T-eB$ phase portraits of the model for various fixed eB, T, μ, and κ_f will also be explored. We will show that for large enough phenomenological value for κ_f, the phenomenon of IMC occurs, i.e., in certain regimes of the parameter space,

[6] See also [51,52] for similar studies.

[7] Assuming the isospin symmetry, we have $M_u = M_d \equiv M$.

[8] The magnetic moment of quarks will be determined by the magnetic moments of protons and neutrons.

the critical temperature (chemical potential) T_c (μ_c) decreases with increasing eB. Moreover, for T-, μ-, eB-dependent κ_f, including the one-loop perturbative correction for α, the phenomenon of reentrance of χSB occurs for certain fixed values of T and μ, and in the regime of weak magnetic fields.

The organization of this paper is as follows. In Sec. II, we will introduce the quark AMM in the magnetized two-flavor NJL model and will determine the one-loop effective action of this model at finite T, μ, and eB. We will also introduce three different sets of the factor $\kappa_f, f = u, d$, mentioned above. In Sec. III A, the T, μ, and eB dependence of the constituent quark mass m will be presented for each fixed κ_f. In Sec. III B, the complete phase portrait of the model will be explored for various fixed κ_f. We will also study, in Sec. III C, the effect of different sets of κ_f on the pressure anisotropies in the longitudinal and transverse directions with respect to the direction of the magnetic field. Eventually, the eB dependence of the magnetization M will be demonstrated, and the effect of κ_f on the product of MB as a function of eB will be studied. Section IV is devoted to our concluding remarks. In Appendix, we will use the constituent quark model, and argue how the constant values of $\kappa_f, f = u, d$ can be determined by the phenomenological data of the magnetic moment of protons and neutrons.

II. THE MODEL

We start with the Lagrangian density of a two-flavor NJL model in the presence of a uniform magnetic field,

$$\mathcal{L} = \bar{\psi}(x)\left(i\gamma^\mu D_\mu - m_0 + \frac{1}{2}\hat{a}\sigma^{\mu\nu}F_{\mu\nu}\right)\psi(x) + G\{[\bar{\psi}(x)\psi(x)]^2 + [\bar{\psi}(x)i\gamma_5\boldsymbol{\tau}\psi(x)]^2\}. \tag{2.1}$$

Here, the Dirac field ψ_f^c carries two flavors, $f \in (1,2) = (u,d)$, and three colors, $c \in (1,2,3) = (r,g,b)$. In the presence of a constant magnetic field, the covariant derivative D_μ is defined by $D_\mu = -\partial_\mu + ie\hat{Q}A_\mu^{\rm ext}$, where the quark charge matrix is given by $\hat{Q} \equiv {\rm diag}(q_u, q_d) = {\rm diag}(2/3, -1/3)$,[9] and the gauge field $A_\mu^{\rm ext} = (0, 0, Bx_1, 0)$ is chosen so that it leads to a uniform magnetic field $\mathbf{B} = B\mathbf{e}_3$, aligned in the third direction. The up and down current quark masses are assumed to be equal, and denoted by $m_0 \equiv m_u = m_d$. This guarantees the isospin symmetry of the theory in the limit of vanishing magnetic field. The latter is introduced by the term proportional to $\sigma_{\mu\nu}F^{\mu\nu}$ in the fermionic kernel of the Lagrangian density $\mathcal{L}$. Here, $\sigma_{\mu\nu} = \frac{i}{2}[\gamma_\mu, \gamma_\nu]$, and the Abelian field strength tensor is given by $F_{\mu\nu} = \partial_{[\mu}A_{\nu]}^{\rm ext}$, with $A_\mu^{\rm ext}$ given above. The proportionality factor $\hat{a}$ is related to the quark AMM (for more details, see Appendix). In the present two-flavor NJL model, $\hat{a}$ is defined by $\hat{a} \equiv \hat{Q}\,\hat{\alpha}\,\mu_B$, where $\hat{Q}$ and $\hat{\alpha} \equiv {\rm diag}(\alpha_u, \alpha_d)$ are 2×2 matrices in the flavor space. At one-loop level, and for a system with isospin symmetry $\alpha_f = \frac{\alpha_e q_f^2}{2\pi}$ for both $f = u, d$ flavors. Here, $\alpha_e = \frac{1}{137}$ is the electromagnetic fine structure constant, and $\mu_B \equiv \frac{e}{2m}$ is given in terms of the electric charge e and the quark constituent mass $m \equiv m_0 + \sigma_0$, where m_0 is the current quark mass and σ_0 the chiral condensate.[10] To introduce the chiral condensate σ_0, let us rewrite the NJL Lagrangian (2.1) in a semi-bosonized form

$$\mathcal{L}_{sb} = \bar{\psi}(x)(i\gamma^\mu D_\mu - m_0 + \hat{a}\sigma^{12}B)\psi(x) - \bar{\psi}(x)(\sigma + i\gamma_5\boldsymbol{\tau}\cdot\boldsymbol{\pi})\psi(x) - \frac{(\sigma^2 + \boldsymbol{\pi}^2)}{4G}, \tag{2.2}$$

where the mesonic fields σ and $\boldsymbol{\pi}$ are defined by

$$\sigma(x) = -2G\bar{\psi}(x)\psi(x), \qquad \boldsymbol{\pi} = -2G\bar{\psi}(x)i\gamma_5\boldsymbol{\tau}\psi(x). \tag{2.3}$$

Here, as in (2.1), G is the NJL mesonic coupling and $\boldsymbol{\tau} = (\tau_1, \tau_2, \tau_3)$ are the Pauli matrices. To arrive at (2.2), $F_{12} = -F_{21} = B$ is used. Integrating out the fermionic degrees of freedom, and using

$$e^{i\Gamma_{\rm eff}[\sigma,\boldsymbol{\pi}]} = \int \mathcal{D}\bar{\psi}\mathcal{D}\psi \exp\left(i\int d^4x\mathcal{L}_{sb}\right), \tag{2.4}$$

the effective action of mesons $(\sigma, \boldsymbol{\pi})$, $\Gamma_{\rm eff} = \Gamma_{\rm eff}^{(0)} + \Gamma_{\rm eff}^{(1)}$ is derived. It is given in terms of a tree-level action

$$\Gamma_{\rm eff}^{(0)}[\sigma, \boldsymbol{\pi}] = -\int d^4x \frac{(\sigma^2 + \boldsymbol{\pi}^2)}{4G}, \tag{2.5}$$

and a one-loop effective action

$$\Gamma_{\rm eff}^{(1)} = -i{\rm Tr}_{\{cf\sigma x\}} \ln[iS_Q^{-1}(\sigma, \boldsymbol{\pi})], \tag{2.6}$$

where the inverse fermion propagator is formally given by

$$iS_Q^{-1}(\sigma, \boldsymbol{\pi}) = i\gamma^\mu D_\mu + \hat{a}\sigma^{12}B - (\bar{m} + i\gamma_5\boldsymbol{\tau}\cdot\boldsymbol{\pi}). \tag{2.7}$$

Here, $\bar{m} = m_0 + \sigma(x)$. Expanding the effective action around a constant configuration $(\sigma_0, \boldsymbol{\pi}_0) = ({\rm const}, \mathbf{0})$ for the mesonic fields $(\sigma, \boldsymbol{\pi})$, the constituent mass $\bar{m}$ turns out to be constant, and can be given by $m = m_0 + \sigma_0$. By carrying out the trace operation over color (c), flavor (f), spinor (σ) degrees of freedom, as well as over the

[9] In this paper, the hat symbol on each quantity denotes its matrix character in the two-dimensional flavor space.

[10] This is in contrast to [51,52], where the Bohr magneton is defined in terms of the current quark mass m_0 (see below).

four-dimensional space-time coordinate (x), the one-loop effective action of this model reads

$$\Gamma^{(1)}_{\text{eff}} = -6i \sum_{q_f=\{\frac{2}{3},-\frac{1}{3}\}} \ln \det{}_x(E^{(p,s)2}_{q_f} - p_0^2). \quad (2.8)$$

Here, the energy spectrum of up and down quarks in the presence of external magnetic fields and for nonvanishing AMM is given by

$$E^{(p,s)}_{q_f} = \sqrt{p_3^2 + [(|q_f eB|[2p+1-s\xi_f] + m^2)^{1/2} - s\kappa_f q_f eB]^2}, \quad (2.9)$$

where $p \geq 0$ labels the Landau levels, and $s = \pm 1$ stands for the spin of the quarks. Moreover, $\xi_f \equiv \text{sgn}(q_f eB)$ and $\kappa_f \equiv \frac{\alpha_f}{2m}$, with $f = u, d$. The energy $E^{(n,s)}_{q_f}$ arises either by computing the fermion determinant of the present two-flavor NJL model including the quark AMM, or by solving the modified Dirac equation $(\gamma \cdot \Pi - m + \frac{1}{2}\hat{a}\sigma^{\mu\nu}F_{\mu\nu})\psi(x) = 0$, with $\Pi_\mu \equiv i\partial_\mu - e\hat{Q}A^{\text{ext}}_\mu$, using, e.g., the Ritus eigenfunction method [59]. Following this method, which is descibed also in [60] for two- and four-dimensional space-time, it turns out that for nonvanishing fermion AMM, only the energy eigenvalues of the Dirac operator are modified, while the Ritus eigenfunctions remain the same as for vanishing AMM. Let us notice that, the additional $\hat{a}\sigma^{\mu\nu}F_{\mu\nu}$ term in the Dirac operator commutes with $(\gamma \cdot \Pi)^2$. This is why the modified Dirac operator $\gamma \cdot \Pi - m + \frac{1}{2}\hat{a}\sigma^{\mu\nu}F_{\mu\nu}$ has the same eigenfunctions as the ordinary Dirac $\gamma \cdot \Pi - m$ for vanishing AMM.

Let us compare, at this stage, the energy dispersion (2.9), with the energy dispersion (1.1) appearing also in [51–53].[11] According to Schwinger [54], T_f is linear in B, and is given by $T^{\text{sch}}_f \equiv \alpha_f q_f \mu_B B$. Plugging $\mu_B = \frac{e}{2m}$ into this relation and using $\kappa_f = \frac{\alpha_f}{2m}$, we obtain $T^{\text{sch}}_f = \kappa_f q_f eB$, which appears also in (2.9). Thus, starting from the above T^{sch}_f., the two energy dispersion relations (2.9) and (1.1) are equal. The Schwinger linear-in-B ansatz for AMM is recently discussed in the literature [51,52]. In particular, it is shown, that this ansatz is only valid in the weak-field limit $eB \ll m_0^2$. In the present paper, however, we will use it for the whole range of eB. To explain this apparent discrepancy, let us notice that the crucial difference between our approach and the one presented in [51,52], is that in our approach the Bohr magneton μ_B is defined in terms of the constituent quark mass $m = m_0 + \sigma_0$, with m_0 the current quark mass and σ_0 the chiral condensate, while in [51,52], the Schwinger ansatz is defined in terms of $\mu^0_B \equiv \frac{e}{2m_0}$, and is independent of σ_0. Having this in mind, we expect, that the difficulties related to the Schwinger linear ansatz with μ^0_B, described in [51,52], do not occur in our work.

As described in Sec. I, in the present paper, the quark AMM will be introduced in the framework of a constituent quark model. This is in contrast to [50–53], where a dynamical symmetry breaking is responsible for its generation. In [50], for instance, the quark AMM is dynamically induced through a nonvanishing spin-one condensate. Here, starting from a massless theory, it is shown that since a nonperturbative mechanism of quark pairing, mainly in the LLL, is responsible for the dynamical generation of AMM, the Schwinger linear-in-B ansatz, $T^{\text{sch}}_f = \alpha_f q_f \mu^0_B B$, is not even valid in the aforementioned weak-field approximation.[12] In the present paper, however, in contrast to [50], we do not start with a massless Dirac theory. Moreover, we will work, in contrast to [50], in the supercritical regime of the NJL model, i.e., we will choose the NJL coupling G in such a way that the model exhibits a dynamical mass, even for zero eB. We will consider the contributions of all Landau level, and will neither restrict ourselves to LLL, as in [50], nor to one-loop approximation in the LLL, as in [51,52]. Hence, starting from the Schwinger linear ansatz with μ_B instead of μ^0_B seems to be reasonable within the constituent quark model. Here, although the quark AMM is not dynamically generated, as in [50–52], but it is related to the dynamically generated quark mass m through the nonperturbative (effective) Bohr magneton [53] μ_B in $T^{\text{sch}}_f \equiv \alpha_f q_f \mu_B B$.

The constituent quark mass m is determined by minimizing the thermodynamic (one-loop effective) potential, arising from (2.8). For a constant configuration σ_0, the one-loop effective potential of the theory is given by performing the remaining determinant over the coordinate space in (2.8). This leads to the one-loop effective potential Ω_{eff}., defined by $\Omega^{(1)}_{\text{eff}} \equiv -\mathcal{V}^{-1}\Gamma^{(1)}_{\text{eff}}$, where $\mathcal{V}$ denotes the four-dimensional space-time volume. In momentum space, the aforementioned determinant is evaluated by the standard replacement

$$\int \frac{d^4p}{(2\pi)^4} f(p_0, \mathbf{p}) \to \frac{|q_f eB|}{\beta} \times \sum_{n=-\infty}^{+\infty} \sum_{p=0}^{+\infty} \sum_{s=\pm 1} \int \frac{dp_3}{8\pi^3} f(i\omega_n - \mu, p, s, p_3), \quad (2.10)$$

where temperature T and chemical potential μ are introduced by replacing p_0 with $p_0 = i\omega_n - \mu$. Here, the

[11] We have slightly changed the notations of Ferrer et al. in [51–53], to be able to compare their results with ours. In particular, to consider the multiflavor nature of the NJL model in the present paper, we have inserted q_f wherever it was necessary.

[12] The LLL approximation is allowed only in the strong-field limit $eB \gg m_0^2$. Moreover, the nonperturbative result for AMM, arising in the LLL approximation [50] is nonanalytic, and cannot be Taylor expanded in the orders of B.

Matsubara frequencies $\omega_n \equiv \frac{(2n+1)\pi}{\beta}$ with $\beta \equiv T^{-1}$ are labeled by n. After performing the sum over n, the effective potential of the two-flavor NJL model, including the tree-level and the one-loop part is given by

$$\begin{aligned}\Omega_{\text{eff}}(m;T,\mu,eB) &= \frac{(m-m_0)^2}{4G} - 3\sum_{q_f=\{\frac{2}{3},-\frac{1}{3}\}}\frac{|q_f eB|}{\beta} \\ &\times \sum_{p=0}^{+\infty}\sum_{s=\pm 1}\int\frac{dp_3}{4\pi^2}\{\beta E_{q_f}^{(p,s)} + \ln\left(1+e^{-\beta(E_{q_f}^{(p,s)}+\mu)}\right) \\ &+ \ln\left(1+e^{-\beta(E_{q_f}^{(p,s)}-\mu)}\right)\}. \end{aligned} \tag{2.11}$$

In the rest of this paper, we will use the above effective potential to study the phase diagram of the magnetized two-flavor NJL model at finite (T,μ,eB) and for a given value of $\kappa_f, f=u,d$. To do this, we will follow two different approaches:

In the first approach, we assume that the value of $\kappa_f = \frac{\alpha_f}{2m}$, appearing in the quark energy dispersion relation $E_{q_f}^{(p,s)}$ from (2.9), is constant and independent of (T,μ,eB). Minimizing the effective potential Ω_{eff}. from (2.11) with respect to m, we will numerically determine the constituent quark mass m as a function of (T,μ,eB) and for a fixed value of $\kappa_f, f=u,d$. In this approach, $\alpha_f = 2m\kappa_f$ will depend on (T,μ,eB) only through the constituent mass m. To fix $\hat{\kappa}$, we will follow the method described in Appendix. Here, two different sets of constant $\hat{\kappa}_i = \text{diag}(\kappa_u^{(i)}, \kappa_d^{(i)})$, $i=1,2$ are introduced, which are compatible with the constituent quark model [see (A10) and (A12)]. To have a sizable quark AMM, we will use

$$\begin{aligned}\kappa_u^{(1)} &= 0.29016\ \text{GeV}^{-1}, \\ \kappa_d^{(1)} &= 0.35986\ \text{GeV}^{-1}, \end{aligned} \tag{2.12}$$

[see also (A9)]. The second set yields smaller values of $\alpha_f, f=u,d$,

$$\begin{aligned}\kappa_u^{(2)} &= 0.00995\ \text{GeV}^{-1}, \\ \kappa_d^{(2)} &= 0.07975\ \text{GeV}^{-1}, \end{aligned} \tag{2.13}$$

[see also (A11)]. In Sec. III, we will in particular show, that once $\hat{\kappa}$ in (2.9) is chosen to be $\hat{\kappa}_1$ from (2.12), the phenomenon of IMC occurs in the phase diagram of our two-flavor magnetized NJL model.

In the second approach, we will consider the leading one-loop correction to the quark (electromagnetic) AMM at nonzero T and vanishing μ and eB. Let us denote it by $\alpha_f = \alpha_f^{\text{1-loop}}(T,\mu=0,eB=0)$ (see below). To determine the constituent quark mass m, we will insert $\kappa_f = \frac{\alpha_f}{2m}$ with $\alpha_f = \alpha_f^{\text{1-loop}}$ into (2.9), and then (2.9) into the one-loop effective potential (2.11), whose minima will then lead to T-, μ-, and eB-dependent m.

To determine the one-loop correction $\alpha_f^{\text{1-loop}}$, we use the result presented in [57,58] for thermal QED, and generalize it to the case of QCD. In [58], the anomalous magnetic moment of electrons at one- and two-loop orders are computed at finite T, zero μ and for vanishing eB. Since in our model the electromagnetic coupling between the quarks and the external photons is to be considered, the QED results presented in [58] are directly applicable for our QCD-like model, including quarks with different flavors $f=u,d$. It is enough to multiply the corresponding QED result with q_f^2, where q_f is the charge of the fth quark flavor. We therefore have

$$\kappa_f(T,\mu,eB) = \frac{\alpha_f^{\text{1-loop}}(T,\mu=0,eB=0)}{2m(T,\mu,eB)}, \tag{2.14}$$

with the one-loop contribution

$$\alpha_f^{\text{1-loop}}(T,\mu=0,eB=0) = q_f^2\mathcal{F}(m^{(0)}\beta), \tag{2.15}$$

for $f=u,d$. Here, $m^{(0)} \equiv m(T=\mu=eB=0)$ is the constituent quark mass at zero (T,μ,eB), and

$$\mathcal{F}(z,\alpha_e) = \frac{\alpha_e}{2\pi} - \frac{2\alpha_e}{3}\left(\frac{\pi}{2z^2}[1-\mathcal{C}(z)] + \mathcal{A}(z) - \mathcal{B}(z)\right), \tag{2.16}$$

with α_e the electromagnetic fine structure constant, and the functions $\mathcal{A},\mathcal{B}$ and $\mathcal{C}$ given by

$$\begin{aligned}\mathcal{A}(z) &= \frac{2T}{\pi m}\ln(1+e^{-z}), \\ \mathcal{B}(z) &= \sum_{n=1}^{\infty}(-1)^n\text{Ei}(-nz), \\ \mathcal{C}(z) &= \frac{6}{\pi}\sum_{n=1}^{\infty}\frac{(-1)^n}{n^2}e^{-nz}. \end{aligned} \tag{2.17}$$

Here, $\text{Ei}(z)$ is the well-known exponential integral function, defined by

$$\text{Ei}(z) = -\int_{-z}^{\infty}\frac{e^{-t}}{t}dt. \tag{2.18}$$

Let us notice, that since $\alpha_e \ll 1$, the one-loop contribution $\alpha_f^{\text{1-loop}}$ is indeed the dominant radiative correction. This is why, the higher order loop corrections will be neglected in the present paper. Moreover, in order to find the range of reliability of the linear-in-B ansatz for the quark AMM, $\hat{T} = \hat{\kappa}\,\hat{Q}\,eB$ from (1.1), with the above listed $\hat{\kappa}$s from

(2.12)–(2.14), the test originally introduced in [51] is to be performed. To do this, we have to consider the rest energy of the quarks in the LLL, which is given by

$$E_{q_u}^{(0,1)} = |m - \kappa_u q_u eB|, \qquad E_{q_d}^{(0,-1)} = |m - \kappa_d q_d eB|, \tag{2.19}$$

for up and down quarks. Plugging $\kappa_f, f = u, d$ from (2.12)–(2.14) in the above relation, and looking for the dependence of $E_{q_u}^{(0,1)}/m$ and $E_{q_d}^{(0,-1)}/m$ on the dimensionless ratio $2eB/m^2$, it turns out that the above ansatz $\hat{T} = \hat{\kappa}\,\hat{Q}\,eB$ is reliable up to $eB \sim 1.2$ GeV^2, in contrast to the Schwinger original ansatz $\hat{T} = \hat{\alpha}\,\hat{Q}\,\mu_B^0 B$ in terms of the bare Bohr magneton $\mu_B^0 = \frac{e}{2m_0}$. In this paper, we will particularly restrict ourselves to the regime $eB \in [0, 0.8]$ GeV^2, which is within the reliability range of the linear ansatz, and which turns out to be relevant for the phenomenology of heavy ion experiments.

III. NUMERICAL RESULTS

The aim of this paper is to study the effect of the quark AMM on a hot and magnetized quark matter. To this purpose, the thermodynamic potential of a two-flavor NJL model is determined in the previous section. It mimics the thermodynamic properties of quark matter at high temperature, finite density and in the presence of an external magnetic field. The quantity, $\hat{\alpha} = \mathrm{diag}(\alpha_u, \alpha_d)$, which is introduced in the original Lagrangian (2.1) as the coefficient corresponding to the spin-field interaction term $\sigma^{\mu\nu}F_{\mu\nu}$, appears in the quark energy dispersion relation $E_{q_f}^{(p,s)}$ from (2.9) in the one-loop effective potential (2.11), essentially in the combination with the constituent quark mass in $\kappa_f = \frac{\alpha_f}{2m}, f = u, d$. Using (2.11), it is now possible to determine the thermodynamic properties of the present quark model, and, in particular, to study various effects of the quark AMM on hot and magnetized quark matter.

As we have discussed in Sec. I, the most important effect of the presence of a uniform magnetic field on a system of charged fermions is the phenomenon of MC of chiral symmetry breaking. The first signature of the occurrence of this phenomenon is that the value of the chiral condensate σ_0, and consequently the constituent quark mass $m = m_0 + \sigma_0$ increase with increasing the strength of the external magnetic field eB (see [8,9,22] for detailed discussions). To study the impact of the quark AMM on this specific effect, we will first determine, in Sec. III A 1, the eB dependence of m for zero chemical potential, at a fixed temperature and for three different sets of $\hat{\kappa}$. They will be denoted by κ_1, κ_2 and κ'. Here, κ_1 and κ_2 correspond to the pair $\hat{\kappa}_i = (\kappa_u^{(i)}, \kappa_d^{(i)})$, $i = 1, 2$ from (2.12) and (2.13), and, κ' corresponds to the T-dependent κ_f given in (2.14). The latter includes one-loop perturbative correction to the AMM of quarks and is written as a function of the constituent quark mass m. We will show that whereas for κ_2 and κ', m increases with increasing eB, for κ_1, it decreases with increasing eB. Moreover, in the latter case, the eB dependence of m indicates a first-order phase transition at certain critical eB_c even at $T = \mu = 0$ MeV. This preliminary, unexpected result can be regarded as an indication of the phenomenon of IMC. As is shown in [8,22], the formation of the chiral condensate is suppressed by increasing temperature. In Sec. III A 2, we will study the effect of finite temperature on m for zero chemical potential and various values of eB and $\hat{\kappa}$. We will then compare the corresponding results to κ_1, κ_2 and κ', and elaborate on the difference between the effect of these three different choices for $\hat{\kappa}$.

In Sec. III B, we will then explore the complete phase portrait of our two-flavor hot and magnetized NJL model. The effect of external magnetic fields on the nature of phase transition for $\hat{\kappa} = 0$ GeV^{-1} is previously studied in [8,9,22]. It is, in particular, shown that for zero chemical potential, the critical temperature T_c essentially increases with increasing eB. This can be regarded as another indication of the phenomenon of MC. In Sec. III B 1, we will first study the $T - eB$ phase diagram of our two-flavor hot and magnetized NJL model for zero and nonzero μ and for different $\hat{\kappa}$. We will, in particular, show that the critical temperature of the phase transition decrease with increasing eB once $\hat{\kappa}$ is chosen to be κ_1. This can be regarded as another signature of the aforementioned phenomenon of IMC. In Secs. III B 2 and III B 3, we will then study the $\mu - eB$ and $T - eB$ phase diagrams for various fixed temperatures and magnetic fields, respectively. We will, in particular, compare the results for κ_1 and κ_2 with $\hat{\kappa} = 0$ GeV^{-1}, previously discussed in [8,22].

In Sec. III C, we will finally study the pressure anisotropy between the longitudinal and transverse pressures with respect to the direction of the external magnetic field. Moreover, the eB dependence of the magnetization of the quark matter will be determined for zero and nonzero chemical potential, temperature and for κ_1, κ_2 and κ'. We will show that whereas $\hat{\kappa}$ has essentially no effect on the pressure anisotropy, larger values of $\hat{\kappa}$ leading to sizable values of the quark AMM, suppress the product MB, where M is the quark matter magnetization. The relation between discontinuities appearing in M and the first-order phase transitions will be also discussed.

To perform the numerical analysis in this section, we will essentially use the same method as described in [22] and [8]. In order to determine the constituent quark mass m, we will numerically solve the gap equation corresponding to the thermodynamic potential (2.11)

$$\left.\frac{\partial\Omega_{\mathrm{eff}}(\tilde{m}; T, \mu, eB)}{\partial\tilde{m}}\right|_{\tilde{m}=m} = 0. \tag{3.1}$$

Here, $m = m_0 + \sigma_0$. Our specific choice for free parameters of our model, the ultraviolet (UV) momentum cutoff Λ, the NJL (chiral) coupling constant G, and the current quark mass m_0, is as follows:

$$\Lambda = 0.6643 \text{ GeV}, \qquad G = 4.668 \text{ GeV}^{-2}, \quad \text{and} \quad m_0 = 5 \text{ MeV}. \tag{3.2}$$

The numerical integration over p_3, appearing in (2.11) will be performed using a smooth cutoff function

$$f_\Lambda = \frac{1}{1 + \exp(\frac{|\mathbf{p}|-\Lambda}{A})}, \tag{3.3}$$

for vanishing eB, and

$$f^{(p,s)}_{\Lambda,B} = \frac{1}{1 + \exp\left(\frac{\sqrt{p_3^2+|q_f eBp|[2p+1-s\xi_f]}-\Lambda}{A}\right)}, \tag{3.4}$$

for nonvanishing eB. Here, q_f is the electric charge of the fth quark, p labels the Landau levels, $s = \pm 1$ stands for positive and negative spins of the quarks and $\xi_f = \text{sgn}(q_f eB)$. Moreover, A is a free parameter, which is related to the sharpness of the cutoff scheme. As in [8,9,21,22], A is chosen to be $A = 0.05\Lambda$, where the UV cutoff Λ is given in (3.2). As is described in [25], choosing smooth cutoff functions (3.4) for nonvanishing magnetic fields removes unphysical discontinuities, which appear in many thermodynamical quantities when sharp cutoffs are used. For large enough A, these discontinuities are replaced with smooth oscillations.[13] It shall also be noticed, that apart from A, all other free parameters of the NJL model Λ, G and m_0 are to be fixed in such a way that at $T = \mu = 0$ MeV and for vanishing magnetic fields, the constituent quark mass, the pion mass and decay constant are given by their vacuum values, $m \sim 308$, $m_\pi \sim 139.6$, and $f_\pi \sim 93.35$ MeV, respectively [8,9].

To determine the constituent quark mass m, the global minima of Ω_{eff}. from (2.11) are to be determined. In the chiral limit $m_0 \to 0$, the χSB is characterized by nonvanishing chiral condensate σ_0, and the chiral symmetry restored (χSR) phase by $\sigma_0 = 0$. As it is shown in [8,9,22], in the limit of vanishing m_0 and $\hat{\kappa}$, the presence of external magnetic field induces a first-order phase transition from the χSB into the χSR phase. For $m_0 \neq 0$ and $\hat{\kappa} = 0$ GeV^{-1}, however, we expect a smooth crossover from the chiral χSB, characterized by $\sigma_0 \neq 0$, into the pseudo-chiral symmetry restored (pχSR) phase, characterized by $\sigma_0 = 0$ MeV and $m = m_0$. In Sec. III C, the order of the phase transition for $m_0 \neq 0$ and $\hat{\kappa} \neq 0$ will be elaborated.

[13] As is explained in [21], for smaller values of $A = 0.001\Lambda$ (quasi-sharp cutoff) instead of smooth oscillations, small discontinuities appear in the weak magnetic field regime $eB \lesssim 0.5$ GeV^2.

A. The T and eB dependence of the constituent quark mass m

1. The eB dependence of the constituent quark mass m

In Figs. 1 and 2, the eB dependence of the constituent quark mass $m = m_0 + \sigma_0$ is demonstrated for κ_1, κ_2, and κ' at $\mu = 0$ MeV and at $T = 0$ (Fig. 1) as well as $T = 150$ MeV (Fig. 2). In Figs. 1(a) and 2(a), the results for κ_1 (red dashed lines) are compared with the corresponding data to κ_2 (black solid lines). The latter is then compared with the results for κ' (red dashed lines) in Figs. 1(b) and 2(b). As it turns out, whereas for κ_2 and κ' the constituent quark mass m increases with increasing eB, for κ_1 that yields a sizable quark AMM, m abruptly

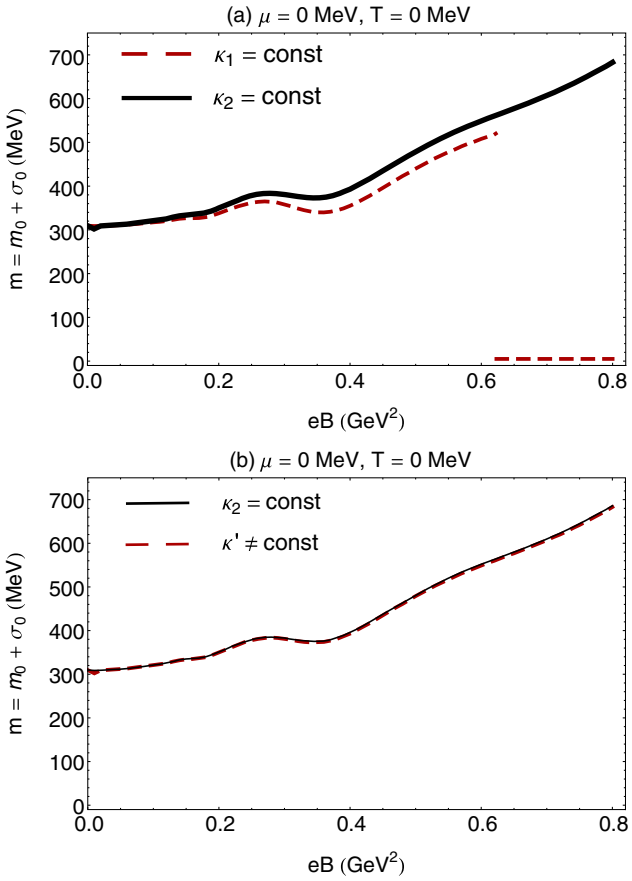

FIG. 1 (color online). (a) The eB dependence of quark constituent mass $m = m_0 + \sigma_0$ is demonstrated for κ_1 (red dashed line) and κ_2 (black solid line) at $T = \mu = 0$ MeV. The behavior of m as a function of eB for κ_1 suggests a first-order phase transition at a critical $eB_c \sim 0.623$ GeV^2. This can be regarded as a possible signature of the phenomenon of IMC. (b) The eB dependence of m is compared for κ_2 (black solid line) and κ' (red dashed line) at $T = \mu = 0$ MeV. The fact that m increases with increasing eB is related to the phenomenon of MC.

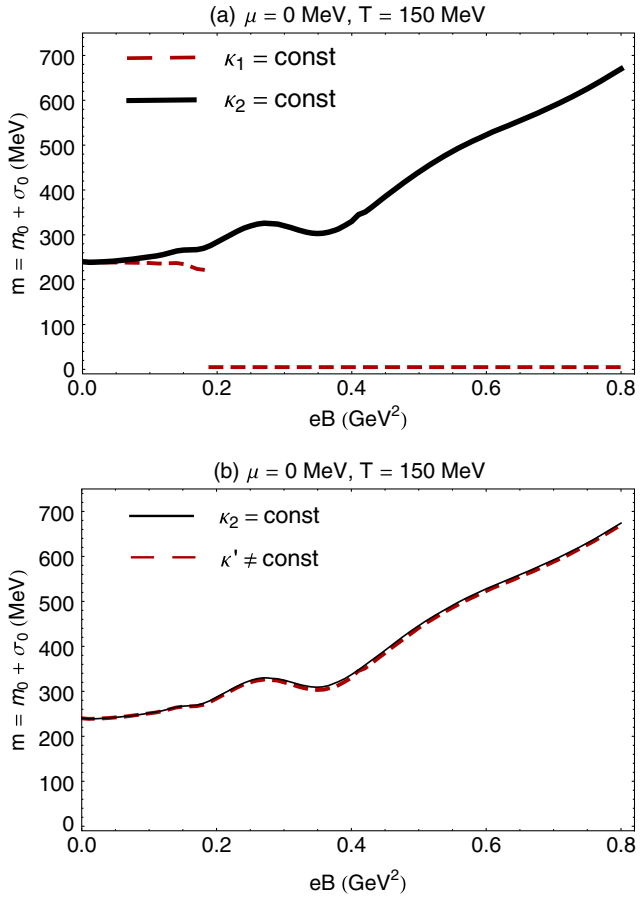

FIG. 2 (color online). (a) The eB dependence of quark constituent mass $m = m_0 + \sigma_0$ is demonstrated for κ_1 (red dashed line) and κ_2 (black solid line) at $T = 150$ MeV and $\mu = 0$ MeV. As in the $T = 0$ MeV case of Fig. 1, the behavior of m as a function of eB for κ_1 suggests a first-order phase transition at a critical $eB_c \sim 0.190$ GeV^2. This is a possible signature of IMC. (b) The eB dependence of m is compared for κ_2 (black solid line) and κ' (red dashed line) at $T = 150$ MeV and $\mu = 0$ MeV.

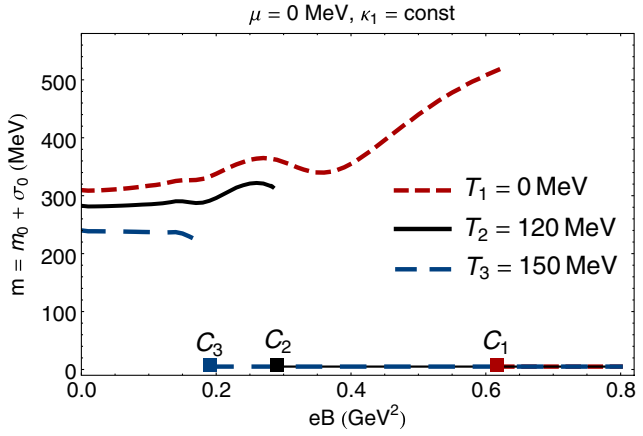

FIG. 3 (color online). The eB dependence of the constituent quark mass $m = m_0 + \sigma_0$ is demonstrated for $\mu = 0$ MeV and at different temperatures $T_1 = 0$, $T_2 = 120$, and $T_3 = 150$ MeV. Here, $\hat{\kappa}$ is held fixed to be κ_1. The critical magnetic fields corresponding to T_i, $i = 1, 2, 3$ MeV are denoted by C_1, C_2, and C_3, respectively. They are given by $eB_{c_1} = 0.623$, $eB_{c_2} = 0.285$, and $eB_{c_3} = 0.190$ GeV^2. As it turns out, eB_c deceases with increasing T. This is an indication of IMC, that apparently occurs once the quark AMM is large enough.

decreases at a certain critical magnetic field eB_c to a value $m = m_0$.[14] This indicates that once $\hat{\kappa}$ is chosen to be κ_1, for $\mu = 0$ MeV a first-order phase transition occurs at this specific eB_c, which is for $T = 0$ and $T = 150$ MeV equal to $eB_c \sim 0.623$ and $eB_c = 0.190$ GeV^2, respectively. As we have argued above, the fact that m increases with increasing eB can be regarded as one of the most important signatures of the phenomenon of MC, which is supposed to enhance the formation of the quark condensate in the supercritical regime of NJL coupling G. On the other hand, by definition, the phenomenon of IMC is related to the suppression of bound state formation even for large values of eB. Thus, the fact that m decreases with increasing eB for $\hat{\kappa}_1 = (\kappa_u^{(1)}, \kappa_d^{(1)})$ from (2.12) is related to the phenomenon of IMC for $\mu = 0$ MeV and $T = 0, 150$ MeV.

To study the effect of temperature on the aforementioned critical magnetic field eB_c for κ_1, the eB dependence of m is considered in Fig. 3 for three different temperatures, $T_1 = 0$ (red dashed line), $T_2 = 120$ (black solid line), and $T_3 = 150$ MeV (blue dashed line). The critical magnetic fields corresponding to these temperatures are denoted by C_1, C_2, and C_3. Numerically, they are given by $eB_{c_1} \sim 0.623$ GeV^2, $eB_{c_2} \sim 0.285$ GeV^2 and $eB_{c_3} \sim 0.190$ GeV^2. It turns out, that eB_c decreases with increasing T. This can again be considered as a signature of the phenomenon of IMC, which seems to occur once the quark AMM is large enough. Later, we will study the $T - eB$ phase diagram for $\mu = 0$ MeV and κ_1, κ_2, and κ'. We will show, that in contrast to the case of κ_2 and κ', the critical temperature corresponding to κ_1 decreases with increasing eB (see Fig. 8 for more details).

According to the results from [22], in the chiral limit $m_0 \to 0$, the two-flavor NJL model at finite T and zero μ and eB exhibits a second-order phase at $T_c \sim 200$ MeV, and for nonvanishing eB, T_c increases with increasing eB up to $T_c \sim 360$ MeV for $eB = 0.7$ GeV^2 [22]. Hence, the temperature interval $T \in [200, 360]$ MeV can be regarded as the regime of phase transition of this QCD-like model. On the other hand, as it is shown in [8], for $m_0 \neq 0$, the above-mentioned second-order phase transition turns into a smooth crossover. In this case the temperature interval $T \in [200, 360]$ MeV indicates the crossover region from the χSB into the pχSR phase. In Figs. 4 and 5, the eB dependence of the constituent quark mass m is

[14] As aforementioned, for nonzero current quark mass m_0, m turns out to be equal to m_0 after the transition into the pχSR phase is occurred.

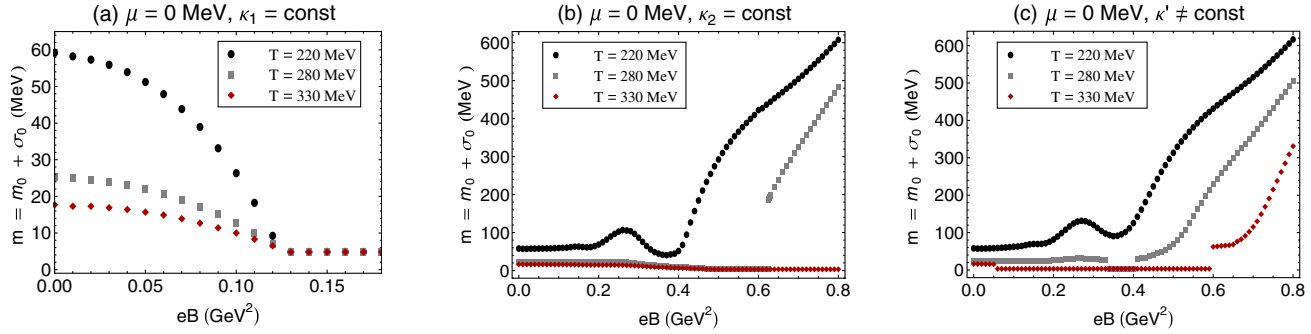

FIG. 4 (color online). The eB dependence of the constituent quark mass $m = m_0 + \sigma_0$ is demonstrated for $\mu = 0$ MeV at different temperatures, $T = 220$ (black circles), $T = 280$ (gray squares), $T = 330$ MeV (red diamonds), and for κ_1 (panel a), κ_2 (panel b), and κ' (panel c). The eB dependence of m for κ_2 and κ' at $T > 200$ MeV turns out to be different at $T < 200$ MeV, demonstrated in Figs. 1 and 2. The data for κ_2, $\mu = 0$ MeV, and $T = 280$ MeV are characterized by a critical $eB_c \sim 0.625$ GeV^2 (panel b), and those for κ' are characterized by two critical $eB_{c_1} \sim 0.33$, and $eB_{c_2} \sim 0.41$ GeV^2 (panel c). Similarly, the data for κ' for $\mu = 0$ MeV, and $T = 330$ MeV are characterized by two critical $eB_{c_1} \sim 0.05$ and $eB_{c_2} \sim 0.6$ GeV^2 (panel c). The appearance of two critical eBs is, in particular, an indication of the phenomenon of reentrance from the pχSR into χSB phase.

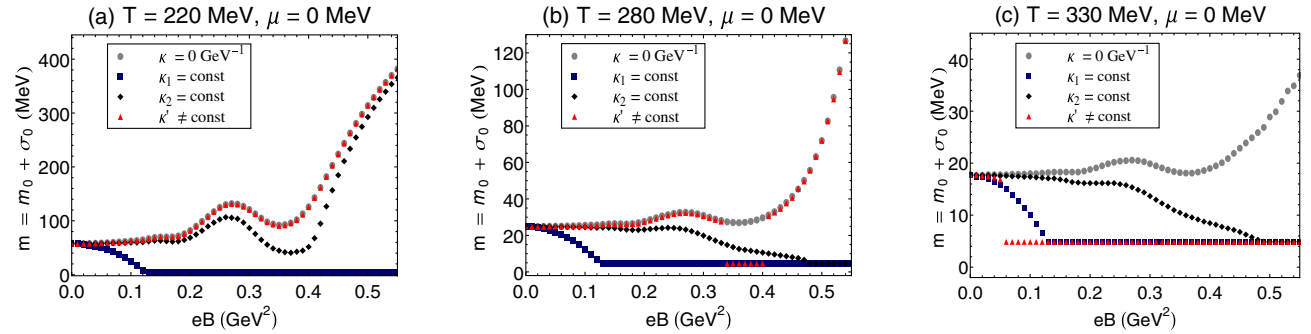

FIG. 5 (color online). The eB dependence of the constituent quark mass $m = m_0 + \sigma_0$ is demonstrated for $\mu = 0$ MeV, at $T = 220$ (panel a), $T = 280$ (panel b), and $T = 330$ MeV (panel c). The data for different $\hat{\kappa}$, including $\hat{\kappa} = 0$ GeV^{-1} (gray circles), κ_1 (blue squares), κ_2 (black diamonds), and κ' (red triangles), are compared. The difference between the data for $\hat{\kappa} = 0$ GeV^{-1} and κ' maximizes with increasing temperature. The data for κ_2 for $T \geq 280$ MeV indicate a crossover transition from the χSB into the pχSR phase. The eB dependence of m for κ' at $T = 330$ MeV and $\mu = 0$ MeV is similar to the case of κ_1. The data for κ' are characterized by a critical magnetic field $eB_c \sim 0.05$ GeV^2.

demonstrated at $T = 220, 280, 330$ MeV, for $\mu = 0$ MeV and different κs in the crossover regime of our model. Comparing the results for κ_1 in Fig. 3 at $T < 200$ MeV with the results for κ_1 at $T > 200$ MeV from Fig. 4(a), it turns out that the first-order phase transition, appearing at $T < 200$ MeV, turns into a smooth crossover at $T > 200$ MeV. As concerns the results for κ_2 and κ', we observed in Figs. 1(b) and 2(b), that at $T < 200$ MeV, m increases with increasing eB. At $T > 200$ MeV, however, the situation changes. Whereas for $T = 220$ MeV, m increases with increasing eB for both κ_2 and κ' [see the black circles in Figs. 4(b) and 4(c)], at $T = 280$ and $T = 330$ MeV, m decreases first with eB and then suddenly increases for certain critical magnetic fields [see gray squares for $T = 280$ MeV and red diamonds for $T = 330$ MeV in Figs. 4(b) and 4(c)]. Comparing the data for κ_2 and κ' at $T = 280$ MeV [gray squares in Figs. 4(b) and 4(c)], it turns out that for κ_2, one and for κ' two critical magnetic fields exist. They are given by $eB_c \sim 0.625$ GeV^2 for κ_2 and $eB_{c_1} \sim 0.33$ GeV^2 and $eB_{c_2} \sim 0.41$ GeV^2 for κ'. This means that in the latter case, the system is first in the χSB phase, enters at eB_{c_1} the pχSR phase, and reenters the χSB phase at eB_{c_2} (see Fig. 8 for more detailed analysis of the phase transitions for different $\hat{\kappa}$ and the discussions related to the phenomenon of reentrance from the χSB into the pχSR phase). Let us now compare the data corresponding to κ_2 and κ' at $T = 330$ MeV and $\mu = 0$ MeV in Figs. 4(b) and 4(c) (red diamonds). It turns out, that for κ_2, m decreases with increasing eB in the whole range $eB \in [0, 0.8]$ GeV^2, while, for κ', there are two critical magnetic fields $eB_{c_1} \sim 0.05$ GeV^2 and $eB_{c_2} \sim 0.6$ GeV^2. In other words, for κ', the quark matter is first in the χSB phase, enters the pχSR phase, and then reenters the χSB phase. Our findings in Fig. 8 confirm this conclusion.

In Fig. 5, we compare the eB dependence of m for different $\hat{\kappa}$: $\hat{\kappa} = 0$ GeV^{-1} (gray circles), κ_1 (blue squares),

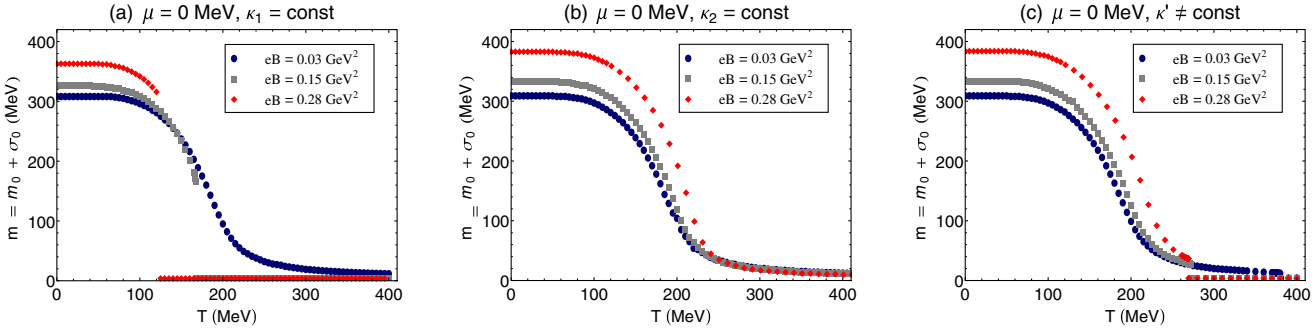

FIG. 6 (color online). The T dependence of the constituent quark mass $m = m_0 + \sigma_0$ is demonstrated for $\mu = 0$ and T-independent κ_1 (panel a), κ_2 (panel b), and κ' (panel c) for $eB = 0.03$ (blue circles), $eB = 0.15$ (gray squares), and $eB = 0.28$ GeV^2 (red diamonds). Discontinuous decreasing of m with increasing T indicates a first-order phase transition from the χSB into the pχSR phase. This occurs, in particular, for κ_1, that leads to a sizable quark AMM.

κ_2 (black diamonds), κ' (red triangles), for $\mu = 0$ MeV, and at $T = 220$ [Fig. 5(a)], $T = 280$ [Fig. 5(b)], and $T = 330$ MeV [Fig. 5(c)]. We limited ourselves to the regime $eB \in [0, 0.5]$ GeV^2 in order to magnify the difference in the eB dependence of m, especially for $\hat{\kappa} = 0$ GeV^{-1}, κ_2, and κ'. According to these results, no difference between the data corresponding to $\hat{\kappa} = 0$ GeV^{-1} and κ' occurs as long as $T \lesssim 250$ MeV. On the other hand, whereas, according to Figs. 1(b) and 2(b), there is no difference between the data corresponding to κ_2 and κ' at $T \lesssim 150$ MeV, at $T > 200$ MeV the eB dependence of m are different for κ_2 and κ'. In particular, it turns out that at $T = 330$ MeV, $\mu = 0$ MeV and for κ', similar to the case of κ_1, m first decreases with increasing eB up to a certain critical $eB_c \sim 0.05$ GeV^2, then suddenly falls down to a value $m = m_0 = 5$ MeV. This is again an indication of the phenomenon of IMC for $\mu = 0$ MeV, at high temperature $T > 280$ MeV and $eB < 0.15$ GeV^2. Let us finally notice that the data for κ_2 in Figs. 5(b) and 5(c) indicates a smooth crossover from the χSB into the pχSR phase in the regime $220 < T < 360$ MeV and $eB < 0.55$ GeV^2 and for $\mu = 0$ MeV (see also Fig. 8 for more details).

2. The T dependence of the constituent quark mass m

According to the results from Figs. 1–5 for fixed μ, eB, and $\hat{\kappa}$, finite temperature suppresses the formation of the chiral condensate σ_0 (see also [8,22]). Consequently, it is expected that m decreases with increasing T. In Fig. 6, the T dependence of the constituent quark mass is demonstrated for $\mu = 0$ MeV, $eB = 0.03$ (blue circles), $eB = 0.15$ (gray squares), $eB = 0.28$ GeV^2 (red diamonds) and different κ_1 (panel a), κ_2 (panel b), and κ' (panel c). As it turns out from the results in Fig. 6(a), whereas for small values of $eB = 0.03$ GeV^2, m decreases continuously with increasing T, for larger values of $eB = 0.15, 0.28$ GeV^2, m decreases with increasing temperature up to a certain critical temperature T_c, which is $T_c \sim 168$ MeV for $eB = 0.15$ GeV^2 and $T_c \sim 120$ MeV for $eB = 0.28$ GeV^2. This behavior indicates a first-order phase transition from the χSB into the pχSR phase for $\mu = 0$ MeV and κ_1. Interestingly, the critical temperature corresponding to this phase transition decreases with increasing eB, which is, as aforementioned, another indication of the phenomenon of IMC once $\hat{\kappa}$ is large enough. For κ_2 and κ', the situation is rather different. According to the results from Fig. 6(b), for κ_2, in contrast to κ_1, m decreases smoothly with increasing T for all values of $eB = 0.03, 0.15, 0.28$ GeV^2. For T-dependent κ', however, whereas for $eB = 0.03$ GeV^2 the constituent quark mass m decreases smoothly with increasing T up to a certain critical temperature $T_c \sim 380$ MeV, for $eB = 0.15$ GeV^2 and $eB = 0.28$ GeV^2, discontinuities occurs at critical temperatures $T_c \sim 272.6$ and $T_c \sim 264$ MeV, respectively.

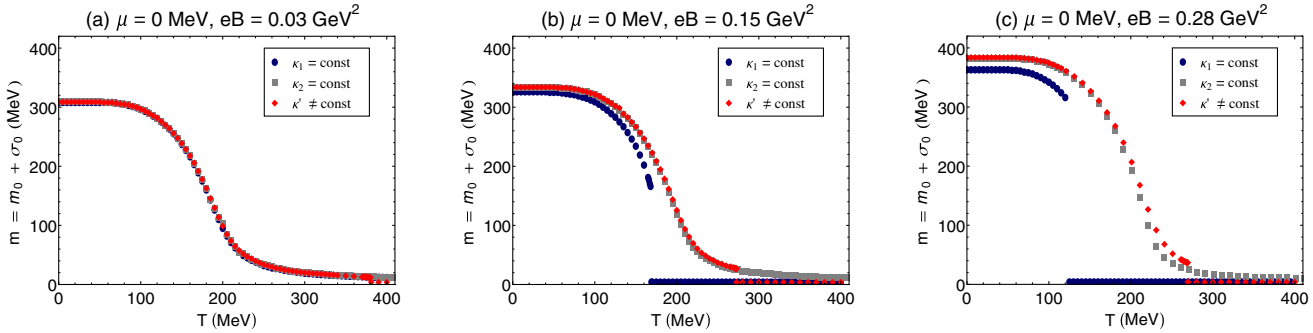

FIG. 7 (color online). The T dependence of the constituent quark mass $m = m_0 + \sigma_0$ is demonstrated for $\mu = 0$ MeV and $eB = 0.03$ (panel a), $eB = 0.15$ (panel b), and $eB = 0.28$ GeV^2 (panel c), for κ_1 (blue circles), κ_2 (gray squares), and κ' (red diamonds).

These kind of discontinuities in the T dependence of m are indications of first-order phase transitions from the χSB into the pχSR phase.

To compare the data for different $\hat{\kappa}$ for fixed μ and eB, the T dependence of m is plotted in Fig. 7 for $\mu = 0$ MeV and $eB = 0.03$ (panel a), $eB = 0.15$ (panel b), and $eB = 0.28$ GeV^2 (panel c) for T-independent κ_1 (blue circles), κ_2 (gray squares), and κ' (red triangles). As it turns out, for small value of $eB = 0.03$ GeV^2, there is almost no difference between the T dependence of m for κ_1, κ_2 and κ', and the transition from the χSB into the pχSR phase turns out to be a smooth crossover. In contrast, according to the results from Figs. 7(b) and 7(c), for $\mu = 0$ MeV and $eB = 0.15$ as well as $eB = 0.28$ GeV^2, whereas in the case of κ_2, m decreases smoothly with increasing T, in two other cases of κ_1 and κ', there exists a certain critical temperature below which m decreases smoothly and above which m turns out to be $m = m_0$ (for the values of T_c, see above). This indicates a first-order phase transition for $eB = 0.15$ and $eB = 0.28$ GeV^2. In what follows, we study the full phase portrait of the two-flavor NJL model for finite (T, μ, eB) and nonzero $\hat{\kappa}$.

B. The phase portrait of hot and magnetized two-flavor NJL model for nonvanishing $\hat{\kappa}$

1. The T-eB phase diagram for various μ and $\hat{\kappa}$

In Fig. 8, the T-eB phase diagram of a hot and magnetized two-flavor NJL model is presented for $\mu = 0$ MeV, constant κ_1, κ_2 and T-, μ-, and eB-dependent

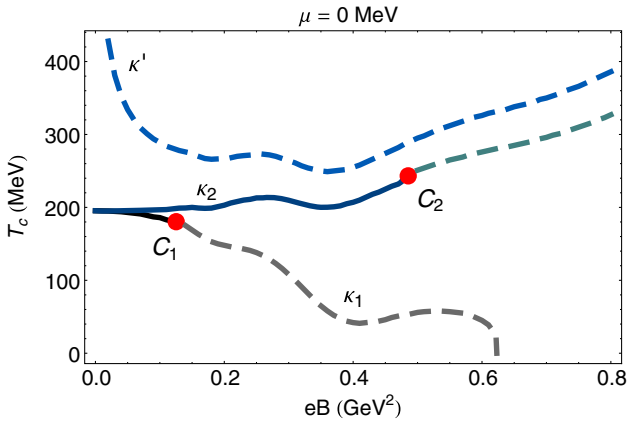

FIG. 8 (color online). The T-eB phase diagram of a hot and magnetized two-flavor NJL model is presented for $\mu = 0$ MeV, κ_1, κ_2, and κ'. The black (for κ_1) and dark blue (for κ_2) solid lines denote the smooth crossovers, and the gray, green and light blue dashed lines the first-order phase transitions for κ_1, κ_2, and κ', respectively. The starting points of the first-order transition lines are denoted by C_1 (for κ_1) and C_2 (for κ_2). The phenomenon of IMC occurs for κ_1 in $eB \in [0, 0.65]$ GeV^2 and κ' in the interval $eB \in [0, 0.25]$ GeV^2. For κ', the dHvA oscillations in the regime $eB \in [0, 0.5]$ GeV^2 lead to the phenomenon of reentrance from the χSB into the pχSR phase.

κ'. The black and dark blue solid lines denote smooth crossover for κ_1 and κ_2, respectively, and the gray, green and light blue dashed lines the first-order phase transitions for κ_1, κ_2, and κ', respectively. The starting points of the first-order phase transitions are denoted by C_1 (for κ_1) and C_2 (for κ_2). As aforementioned, for nonzero m_0, the χSB phase is characterized by $\sigma_0 \neq 0$, and the pχSR phase by $\sigma_0 = 0$ MeV and $m = m_0$. Hence, by definition, the regimes below the critical lines denote the χSB phases and the regimes above them, the pχSR phases. To compare the effect of different choices for $\hat{\kappa}$, let us first consider the transition curve for κ_1. Starting from $eB = 0$ GeV^2, the model exhibits a smooth crossover in the interval $eB \in [0, 0.12]$ GeV^2 (see the black solid line). As it turns out, the crossover temperatures[15] decrease with increasing eB from $T_c \sim 195.4$ MeV for $eB = 0$ GeV^2 to $T_c \sim 181$ MeV for $eB = 0.12$ GeV^2. The end point of the crossover transition line is denoted in Fig. 8 by C_1. For larger values of $eB \in [0.12, 0.623]$ GeV^2, a first-order phase transition occurs (gray dashed line). The critical temperatures for this first-order phase transition decrease with increasing eB. This result confirms our findings from Figs. 1–7. Let us notice, e.g., that for $T = 0$ MeV, the point $eB \sim 0.623$ GeV^2 on the eB axis, is the same eB_{c_1} appearing in Fig. 3 for κ_1 at $T = \mu = 0$ MeV. The fact that, for κ_1, T_c decreases with increasing eB is related to the phenomenon of IMC. This is in contrast to what happens for κ_2. Here, as it turns out, the critical temperature essentially increases with increasing eB in the interval $eB \in [0, 0.8]$ GeV^2. First, in the regime $eB \in [0, 0.478]$ GeV^2, the system exhibits a smooth crossover from the χSB into the pχSR phase (blue solid line). At a certain critical temperature $T = 240$ MeV and magnetic field $eB = 0.478$ GeV^2, denoted by C_2, the crossover transition line turns into a first-order transition line in the regime $eB \in [0.478, 0.8]$ GeV^2 (green dashed line). Let us notice at this stage, that, according to our arguments in [8,9,21,22], the regime $eB > 0.5$ GeV^2 is the regime of LLL dominance. In this regime, in the most cases which we have considered in this paper, the constituent quark mass m as well as the critical temperature T_c monotonically increase with increasing eB. As concerns the T-eB phase diagram for κ' (light blue dashed line). As it turns out, T_c decreases with increasing eB in the regime $eB \in [0.02, 0.24]$ GeV^2, exhibits some oscillations in the regime $eB \in [0.25, 0.37]$ GeV^2 and increases monotonically in the regime $eB \in [0.37, 0.8]$ GeV^2. Hence, an IMC is followed first by some oscillations and then the MC. Moreover, for κ', the transition from the χSB into the pχSB phase is of first-order in the whole regime $eB \in [0.02, 0.8]$ GeV^2 (light blue dashed line).

For κ', because of this special shape of the first-order transition line, another interesting effect occurs. To describe

[15] In the present paper, the crossover temperature T_{cr} is defined by $m(T_{cr}, \mu, eB) \leq e^{-1} m(T = 0, \mu, eB)$.

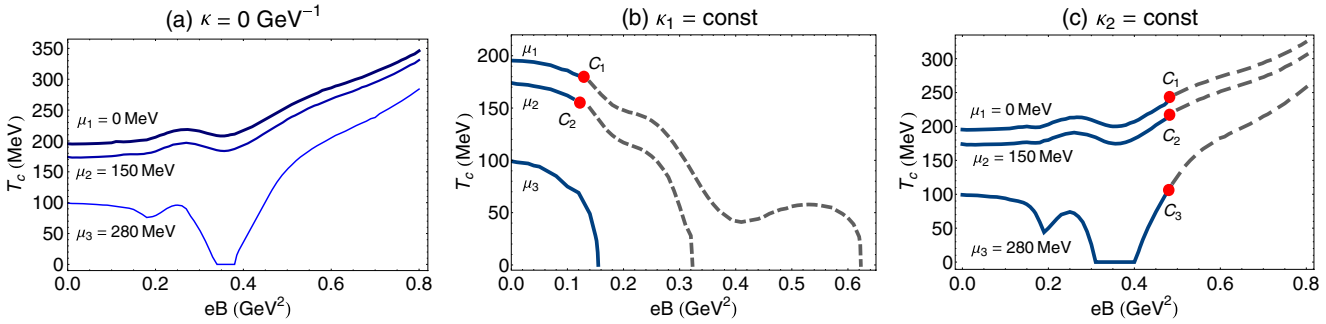

FIG. 9 (color online). The T-eB phase diagram of a hot and magnetized two-flavor NJL model is presented for $\mu_1 = 0$, $\mu_2 = 150$, $\mu_3 = 280$ MeV and $\hat{\kappa} = 0$ GeV^{-1} (panel a), κ_1 (panel b), and κ_2 (panel c). Blue solid lines denote the smooth crossovers from the χSB into the pχSR phase, and gray dashed lines, the first-order phase transitions. The starting points of the first-order transition lines are denoted by C_i, $i = 1, 2, 3$ corresponding to μ_i, $i = 1, 2, 3$. For κ_1, the phenomenon of IMC occurs for $eB \in [0, 0.65]$ GeV^2. For $\hat{\kappa} = 0$ GeV^{-1} and κ_2, the dHvA oscillations in the regime of weak magnetic fields lead to the phenomenon of reentrance from χSB into pχSR phase.

this effect, let us assume the temperature to be $T \sim 300$ MeV. In this case, starting from $eB = 0$ GeV^2, the system is first in the χSB phase, then for $eB \sim 0.1$ GeV^2 a first-order phase transition into the pχSR phase occurs. With increasing the strength of the magnetic field up to $eB \sim 0.55$ GeV^2, the system remains in this phase, and then reenters the χSB phase for $eB > 0.55$ GeV^2 phase. The same phenomenon occurs for all $T \gtrsim 300$ MeV. Let us notice, that the phenomenon of reentrance has been previously observed for nonvanishing μ and vanishing $\hat{\kappa}$ for the same hot and magnetized two-flavor NJL model, as considered in the present paper [22] (see also Figs. 9(a) and 9(b) for $\mu = 280$ and $T \sim 90$ MeV). The results from Fig. 8 show, that for κ', the same phenomenon occurs also for $\mu = 0$ MeV. We believe that this phenomenon, as well as the observed oscillations in the eB dependence of m appearing in Figs. 1, 2, and 5, are essentially related to the dHvA [23] in the weak magnetic field regime $eB \in [0.2, 0.5]$ GeV^2. These effect had been also studied in [21,22,24,25] and most recently in [26]. It occurs whenever Landau levels pass the quark Fermi level. As it turns out, the dHvA oscillations are weakened, once the system enters the LLL dominant regime $eB > 0.5$ GeV^2.

The IMC phenomena exhibited in the eB dependence of the critical line $T_c(B)$ for κ_1 and $\mu = 0$ MeV from Fig. 8, is also observed in lattice QCD simulations for vanishing μ and $\hat{\kappa}$ (i.e., vanishing quark AMM), as discussed in Sec. I [28]. In what follows, a qualitative comparison between our results and the lattice QCD results will be presented. In particular, we will focus on the reliability of the relation

$$T_c(eB; \hat{\kappa}) \propto m(eB, T = \mu = 0; \hat{\kappa}) \qquad (3.5)$$

for vanishing and nonvanishing $\hat{\kappa} = \{\kappa_1, \kappa_2, \kappa'\}$. To do this, it is crucial to notice that the relation (3.5) is only valid for very strong magnetic fields, when the LLL approximation is justified (for the analytical derivation of this relation in the LLL dominant regime of NJL-like models, see, e.g., [61] or more recently [50]). In effective models, which are characterized by a cutoff parameter Λ, the regime of LLL dominance is determined from $\lfloor \frac{\Lambda^2}{|q_f eB|} \rfloor = 0$, as is discussed in [8] for the case of vanishing $\hat{\kappa}$. Here, $\lfloor a \rfloor$ is the greatest integer less than or equal to a. Assuming that the above relation (3.5) is valid for $eB \gtrsim 0.5$ GeV^2, lattice QCD simulations for vanishing $\hat{\kappa}$ already contradict it (see [28] for more details). As concerns the case of nonvanishing $\hat{\kappa}$, a comparison between $m(eB, T = \mu = 0; \hat{\kappa})$ from the plots presented in Fig. 1(b) and $T_c(eB; \hat{\kappa})$ from Fig. 8 shows that for $\hat{\kappa} = \{\kappa_2, \kappa'\}$ the proportionality (3.5) holds in the strong magnetic field regime; as it turns out, $m(eB, T = \mu = 0; \kappa_2)$ and $m(eB, T = \mu = 0; \kappa')$ increase monotonically with increasing eB for $eB \gtrsim 0.5$ GeV^2 [see Fig. 1(b)], and similarly, $T_c(eB, \kappa_2)$ and $T_c(eB, \kappa')$ from Fig. 8 exhibit also the same behavior. For κ_1, leading to large values of nonperturbative quark AMM, the situation is different. In Table I, we have presented the numerical

TABLE I. The eB dependence of $m^{(1)} = m(eB, T = \mu = 0; \kappa_1)$ from Fig. 1(a) is compared with the eB dependence of $T_c^{(1)} = T_c(eB; \kappa_1)$ from Fig. 8 for $eB \geq 0.5$ GeV^2. As it turns out, the relation (3.5) is contradicted in the regime $0.54 \leq eB < 0.623$ GeV^2, where the phenomenon of IMC occurs.

eB in GeV^2	$m^{(1)}$ in MeV	$T_c^{(1)}$ in MeV
0.5	440	56
0.51	448	57
0.52	456	57.5
0.53	464	57.8
0.54	471	57.6
0.55	478	57
0.56	484	56
0.57	491	55
0.58	497	52
0.59	502	49
0.60	508	45
0.61	513	39
0.62	518	27
0.622	520	19
0.623	5	0

results for $m^{(1)} \equiv m(eB, T = \mu = 0; \kappa_1)$ from Fig. 1(a) and $T_c^{(1)} \equiv T_c(eB; \kappa_1)$ from Fig. 8 for $eB \geq 0.5$ GeV^2. As it turns out, whereas $m^{(1)}$ increases first in the regime $0.5 \leq eB < 0.623$ GeV^2 and the suddenly decreases for $eB_c = 0.623$ GeV^2 to its bare value $m_0 = 5$ MeV, the critical temperature $T_c^{(1)}$ first increases for $0.5 \leq eB \leq 0.53$ GeV^2, and then decreases in the regime $0.54 \leq eB < 0.623$ GeV^2. The relation (3.5) is therefore contradicted for κ_1 in the regime $0.54 \leq eB < 0.623$ GeV^2. This seems to be qualitatively in line with the lattice QCD simulations for vanishing $\hat{\kappa}$ in the same magnetic field regime, and, regardless to the value of $\hat{\kappa}$, seems also to be valid whenever the phenomenon of IMC occurs.[16]

To compare the results for vanishing μ from Fig. 8 with the results for nonvanishing μ, the T-eB phase diagram of hot and magnetized NJL model is demonstrated in Fig. 9 for different $\hat{\kappa} = 0$ GeV^{-1} (panel a), κ_1 (panel b), and κ_2 (panel c) and for $\mu_1 = 0, \mu_2 = 150$, and $\mu_3 = 280$ MeV. Solid lines denote the crossover transition lines, and dashed lines the first-order phase transitions from χSB into pχSR phase. Let us first consider Fig. 9(a). We observe, that for $\hat{\kappa} = 0$ GeV^{-1} the crossover transition temperature decreases with increasing μ. The aforementioned dHvA oscillations are stronger for larger μ and disappear in the LLL dominant regime $eB \gtrsim 0.5$ GeV^2. In this regime, T_c increases with increasing eB. This can be regarded as a signature of MC, especially in the LLL dominant regime. For κ_1, however, T_c decreases with increasing eB. Moreover, whereas for $\mu_1 = 0$ and $\mu_2 = 150$ MeV the crossover transitions in the weak magnetic field regime turn into first-order transition lines, for $\mu_3 = 280$ MeV only a crossover transition occurs in the regime $eB \in [0, 0.155]$ GeV^2. The critical points corresponding to $\mu_i, i = 1, 2$ are denoted by $C_i, i = 1, 2$. They are given by $C_1 = (0.12\,\text{GeV}^2, 181\,\text{MeV})$, and $C_2 = (0.12$ GeV^2, 157 MeV). As in the case of $\hat{\kappa} = 0$ GeV^{-1}, T_c decreases with increasing μ for each fixed eB (see also the T-μ phase diagram from Fig. 11). Let us now compare the results for κ_2 from Fig. 9(c) with those for $\hat{\kappa} = 0$ GeV^{-1} from Fig. 9(a). We observe that although the eB dependence of T_c for κ_2, is in general similar to the case with $\hat{\kappa} = 0$ GeV^{-1}, but for κ_2, the crossover transitions, appearing for $\hat{\kappa} = 0$ GeV^{-1} in the whole range of $eB \in [0, 0.8]$ GeV^2 and for all $\mu_i, i = 1, 2, 3$, turn into a first-order phase transitions in the LLL dominant regime $eB \gtrsim 0.5$ GeV^2. The critical points corresponding to $\mu_i, i = 1, 2, 3$ are given by $C_1 = (0.478$ GeV^2, 240 MeV), $C_2 = (0.48$ GeV^2, 215 MeV) and $C_3 = (0.485$ GeV^2, 112 MeV). Similar to the case of $\hat{\kappa} = 0$ GeV^{-1}, the aforementioned phenomenon of reentrance from χSB into pχSR phase occurs also in the case κ_2, in particular, for $\mu = 280$ MeV. Moreover, no dHvA oscillations occur in the LLL dominant regime.

2. The μ-eB phase diagram for various T and $\hat{\kappa}$

In Fig. 10, the μ-eB phase diagram of a hot and magnetized two-flavor NJL model is presented for $T_1 = 0, T_2 = 120$ MeV, as well as for $\hat{\kappa} = 0$ GeV^{-1} (panel a), κ_1 (panel b), and κ_2 (panel c). The black and blue solid lines denote the smooth crossovers for T_1 and T_2, respectively, and the gray dashed lines the first-order phase transitions from the χSB phase (the region below the critical lines) into the pχSR phase (the region above the critical lines). The starting points of the first-order phase transitions are denoted by $C_i, i = 1, 2$ for $T_i, i = 1, 2$. As it turns out, for $\hat{\kappa} = 0$ GeV^{-1}, crossover transitions occur in the whole regime of $eB \in [0, 0.8]$ GeV^2. In contrast, for κ_1 and κ_2, crossover transitions occur up to certain critical points $C_i, i = 1, 2$ and then with increasing eB, they turn into first-order phase transitions. These critical points for κ_1 and $T_1 = 0$, as well as $T_2 = 120$ MeV are, $C_1 = (0.15$ GeV^2, 261 MeV) and $C_2 = (0.13$ GeV^2, 219 MeV) [see Fig. 10(b)]. For κ_2 and $T_1 = 0$, as well as $T_2 = 120$ MeV they are given by $C_1 = (0.44$ GeV^2, 296 MeV) and $C_2 = (0.48$ GeV^2, 274 MeV), respectively [see Fig. 10(c)]. Here, similar to the T-eB phase diagrams, for κ_1 the critical chemical potential μ_c decreases with increasing eB [see Fig. 10(b)]. We conclude therefore that once the quark AMM is sizable enough an inverse magnetic catalysis occurs. Keeping eB fixed, μ_c decreases with increasing T for all values of $\hat{\kappa} \neq 0$ (see also the T-μ phase diagram in Fig. 11). According to the results from Figs. 10(a) and 10(c), for $\hat{\kappa} = 0$ GeV^{-1} and κ_2, the aforementioned dHvA oscillations lead to the phenomenon of reentrance in the regime $\mu \in [285, 335]$ MeV and $\mu \in [260, 330]$ MeV for $T_1 = 0$ MeV and $\hat{\kappa} = 0$ GeV^{-1} and κ_2, respectively. For $T_2 = 120$ MeV, these regimes are given by $\mu \in [245, 270]$ MeV for $\hat{\kappa} = 0$ GeV^{-1} and $\mu \in [240, 265]$ MeV for κ_2.

3. The T-μ phase diagram for various eB and $\hat{\kappa}$

In Fig. 11, the T-μ phase diagram of a hot and magnetized two-flavor NJL model is presented for $eB_1 = 0.03$ (blue lines), $eB_2 = 0.28$ (black lines), and $eB_3 = 0.48$ GeV^2 (gray lines) for $\hat{\kappa} = 0$ GeV^{-1} [Fig. 11(a)], κ_1 [Fig. 11(b)] and κ_2 [Fig. 11(c)]. The solid (dashed) lines denote the crossover (first-order) transitions. The starting points for first-order transition lines are denoted with C (red dots).

The T-μ phase portrait of a two-flavor magnetized NJL model with vanishing quark AMM was already

[16]The quantitative comparison with the lattice data from [28] is beyond the scope of the present paper. To do this, we shall take the lattice data of $T_c(eB)$ for granted, and fix $\hat{\kappa}$ (presumably as a function of the magnetic field) in such a way that they can be reproduced. This will be postponed to future publications. Let us only notice at this stage that similar comparison has been already made in [41], where an appropriate eB-dependent coupling constant for a magnetized Polyakov-loop extended NJL model is considered in such a way, that lattice data are reproduced.

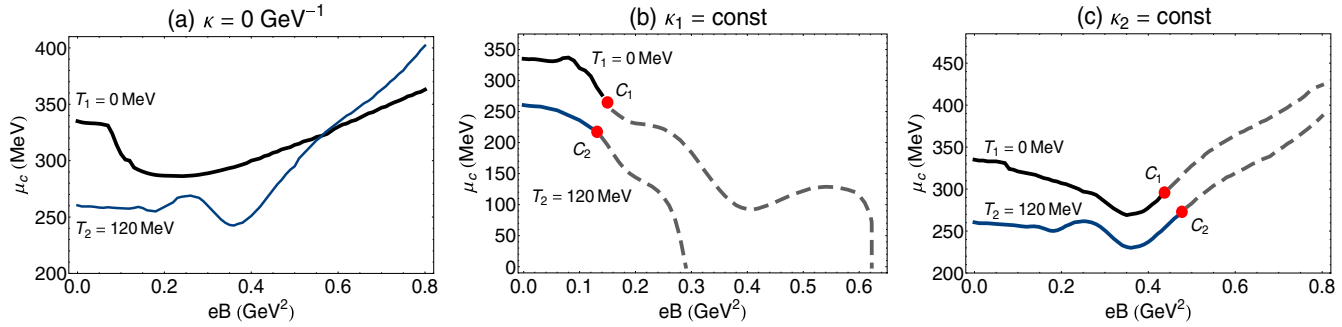

FIG. 10 (color online). The μ-eB phase diagram of a hot and magnetized two-flavor NJL model is presented for $T_1 = 0$, $T_2 = 120$ MeV, and $\hat{\kappa} = 0$ GeV^{-1} (panel a), κ_1 (panel b), and κ_2 (panel c). The black and blue solid lines denote the smooth crossovers from the χSB into the pχSR phase, and gray dashed lines, the first-order phase transitions. The starting points of the first-order transition lines are denoted by $C_i, i = 1, 2$ corresponding to $T_i, i = 1, 2$. For κ_1, the phenomenon of IMC for $eB \in [0, 0.65]$ GeV^2. For $\hat{\kappa} = 0$ GeV^{-1} and κ_2, the dHvA oscillations in the regime of weak magnetic fields lead to the phenomenon of reentrance from χSB into pχSR phase.

demonstrated in [22] for various fixed eB. In [22], in contrast to the case discussed in the present paper, the bare quark mass m_0 was chosen to be zero. Thus, the free parameters of the model were different from the ones given in the present paper [see (3.2)]. The critical lines presented in the T-μ phase portraits of [22] exhibited, in contrast to the critical lines presented in Fig. 11(a), both crossover and first-order transitions, so that certain critical points had been emerged in the T-μ phase space for $\hat{\kappa} = 0$ GeV^{-1} and various eB, and, by increasing the value of eB, it was shifted to higher temperatures and smaller chemical potentials (MC). A comparison of the results presented in [22] with the results demonstrated in Fig. 11(a) for $\hat{\kappa} = 0$ GeV^{-1} shows that obviously the type of the phase transitions and the appearance as well as the position of the critical point are strongly affected by the choice of the free parameters of effective models; as is demonstrated in Fig. 11(a), in contrast to the results presented [22], for all values of $eB_i, i = 1, 2, 3$ only crossover transitions occur.

Let us notice that the results from Fig. 11(a) are compatible with the ones demonstrated in Fig. 9(a) for $\hat{\kappa} = 0$ GeV^{-1}, because, as expected from the results in Figs. 9, for a fixed value of eB, the critical temperature of the chiral phase transition decreases with increasing μ. Different values of $\hat{\kappa}$ do not essentially change this specific feature. A comparison between Fig. 11(a) and Fig. 11(c) shows that although in both cases for a fixed value of μ, the critical temperatures increase with increasing eB (MC), but the critical line of $eB_3 = 0.48$ GeV^2 for κ_2, for instance, displays, in contrast to the same critical line for $\hat{\kappa} = 0$ GeV^{-1}, both types of transitions [compare the gray critical line in Fig. 11(c) with the gray line in Fig. 11(a)]: For κ_2 and $eB_3 = 0.48$ GeV^2, there are two regions where first-order phase transitions (dashed gray lines) occur (at high T and small μ as well as at low T and high μ), and, in between, i.e., for moderate T and μ, the magnetized quark matter exhibits a crossover transition (solid gray line) from the pχSB phase into the pχSR phase. Denoting the end/starting points of the

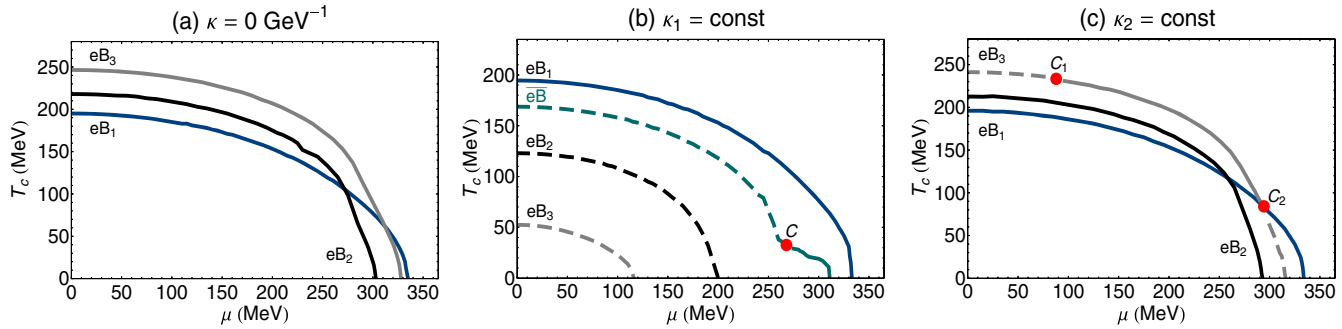

FIG. 11 (color online). The T-μ phase diagram of a hot and magnetized two-flavor NJL model is presented for $eB_1 = 0.03$ (blue lines), $eB_2 = 0.28$ (black lines), and $eB_3 = 0.48$ GeV^2 (gray lines) for $\hat{\kappa} = 0$ GeV^{-1} (panel a), κ_1 (panel b), and κ_2 (panel c). In panel b, the critical line for $\overline{eB} = 0.15$ GeV^2 is also plotted (green dashed and solid lines). The solid (dashed) lines denote the crossover (first-order) transitions. The starting (end) points for first-order transition lines are denoted with C (red dots). In the case of κ_1 the critical point appearing for $\overline{eB} = 0.15$ GeV^2 is shifted to low temperature and large values of chemical potential.

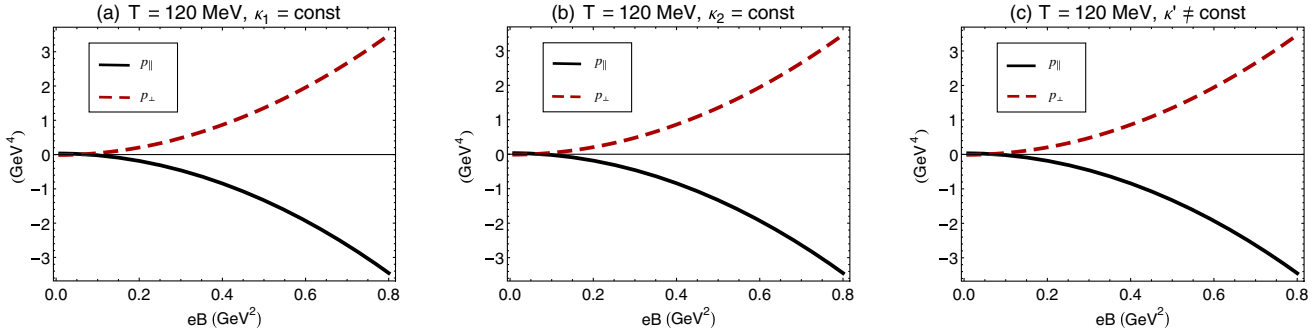

FIG. 12 (color online). The longitudinal (black solid lines) and transverse (red dashed lines) pressures of a two-flavor NJL model, $p_\parallel$ and $p_\perp$, are demonstrated as a function of eB for $T = 120$ MeV, $\mu = 0$ MeV and κ_1 (panel a) and κ_2 (panel b), as well as κ' (panel c). As it turns out, the longitudinal (transverse) pressure decreases (increases) with increasing eB. Different choices for $\hat{\kappa}$ do not significantly affect this specific feature.

first-order phase transitions with $C_i = (\mu_c^{(i)}, T_c^{(i)}), i = 1, 2$ (red dots), we therefore have two critical points for κ_2 and $eB_3 = 0.48$ GeV^2. These are given by $C_1 = (92, 233)$ and $C_2 = (290, 86)$ MeV.

As concerns the case of κ_1 from Fig. 11(b), it turns out that, in contrast to the cases of $\hat{\kappa} = 0$ GeV^{-1} and κ_2 from Figs. 11(a) and 11(c), for fixed μ, the critical temperatures decrease with increasing eB (IMC). Moreover, by comparing the phase portraits of Figs. 11(a) and 11(c) with the phase portrait of Fig. 11(b), it turns out that the crossover transitions for $eB_2 = 0.28$ and $eB_3 = 0.48$ GeV^2 in the cases of $\hat{\kappa} = 0$ GeV^{-1} and κ_2, turn into a first-order phase transition for κ_1 and the same eBs, and, as a consequence of IMC for κ_1, the pχSB phase is shifted to the region with lower temperatures and lower chemical potentials [compare the dashed black and gray lines in Fig. 11(b) with the solid black and gray lines in Figs. 11(a) and 11(c)]. These results confirm our findings in Figs. 8, 9(b), and 10(b), and can be regarded as one of the main indications of the effect of large nonperturbative quark AMM on QCD phase diagram. To answer whether a critical point emerges for κ_1, we have plotted the critical line for $\overline{eB} = 0.15$ GeV^2, as a typical example [see the green dashed and solid lines in Fig. 11(b)]. As it turns out, a critical point emerges at $C = (\mu_c, T_c) = (270, 33)$ MeV at the end of a first-order transition line [see the green dashed line in Fig. 11(b)]. This latter result is also compatible with the results presented in Fig. 9(b).

C. The pressure anisotropy and magnetization of quark matter for nonvanishing $\hat{\kappa}$

Nonvanishing magnetic fields break the Lorentz invariance, and induce certain anisotropies in the pressure of a hot and magnetized quark matter with respect to the direction of the background field. The eB dependence of pressure of a hot and magnetized quark matter for vanishing and nonvanishing $\hat{\kappa}$ has been already demonstrated in [51,52,62], where the effect of the quark AMM in the strong magnetic field regime $eB > m_0^2$ is compared with the weak-field AMM by Schwinger [54]. The anisotropy in the pressure of hot and magnetized QCD is also investigated recently in [32] in the framework of lattice gauge theory. Let us denote the longitudinal and transverse pressures with respect to the direction of the magnetic field by $p_\parallel$ and $p_\perp$. According to [52,62], they are defined by

$$p_\parallel \equiv -\Omega_{\rm eff}^{\rm min}(m; T, \mu, eB) - \frac{B^2}{2},$$
$$p_\perp \equiv -\Omega_{\rm eff}^{\rm min}(m; T, \mu, eB) - \frac{B^2}{2} + BH, \qquad (3.6)$$

where $\Omega_{\rm eff}^{\rm min}(m; T, \mu, eB)$ is the value of $\Omega_{\rm eff}$ from (2.11), evaluated at the minimum of the effective potential and $B^2/2$ is the classical magnetic energy. Moreover, B and $H \equiv B - M$ are the external and induced magnetic fields, respectively. Here, M is the magnetization of the quark matter, defined by [21]

$$M \equiv -e\frac{\partial\Omega_{\rm eff}(\tilde{m}; T, \mu, eB)}{\partial(eB)}\bigg|_{\tilde{m}=m}. \qquad (3.7)$$

In what follows, we are, in particular, interested in the effect of different sets of $\hat{\kappa}$ on the eB dependence of $p_\parallel$, $p_\perp$ and on the product MB.

In Fig. 12, the longitudinal and transverse pressures, $p_\parallel$ (black solid curves) and $p_\perp$ (red dashed curves) are plotted as functions of eB for $T = 120$ MeV, $\mu = 0$ MeV and κ_1 (panel a), κ_2 (panel b) as well as κ' (panel c).[17] Similar to the results presented in [51], $p_\parallel$ ($p_\perp$) decreases (increases) with increasing eB. As it turns out, different choices of $\hat{\kappa}$ do not significantly affect the final results for the eB dependence of anisotropic pressures. Let us notice at this stage, that there is indeed an ambiguity in determining the longitudinal and transverse pressures in the literature. In [63], for instance, the Maxwell term $B^2/2$ is not considered neither in the effective

[17] In Fig. 12, the anisotropic pressures from (3.6) are slightly modified by $p_\parallel = -\Omega_{\rm eff}^{\rm min} - e^{-2}b^2/2$ and $p_\perp = -\Omega_{\rm eff}^{\rm min} + e^{-2}b^2/2 - \tilde{M}b$ with $b \equiv eB$ and $\tilde{M} \equiv e^{-1}M$. Here, e^2 is replaced by $e^2 = 4\pi\alpha_e$, with $\alpha_e = 1/137$ the electromagnetic fine structure constant.

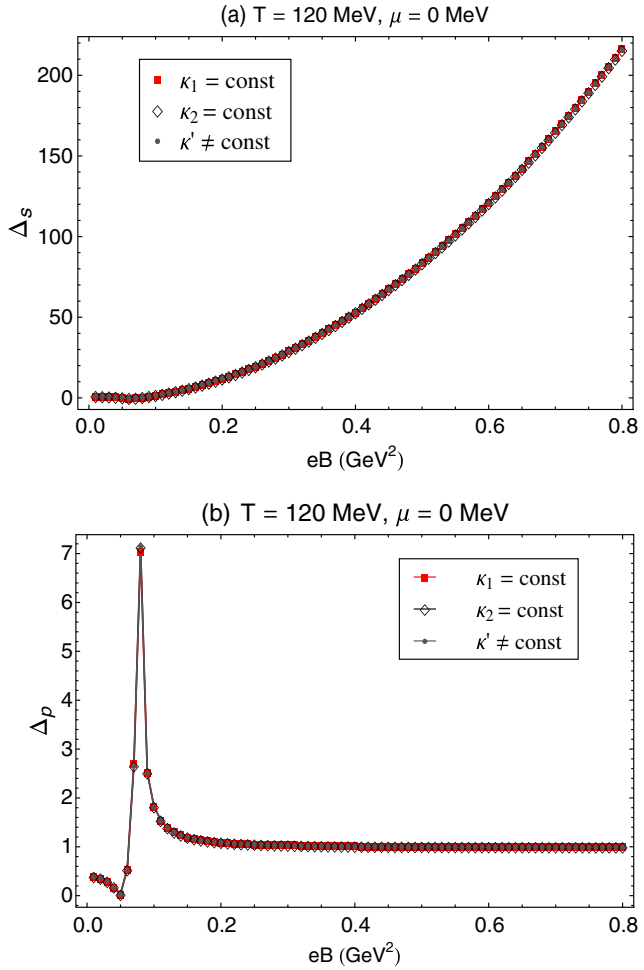

FIG. 13 (color online). The quantities Δ_s and Δ_p, defined in (3.8) and (3.9), are plotted as functions of eB, at $T = 120$ MeV and for $\mu = 0$ MeV as well as κ_1 (red squares), κ_2 (empty diamonds), and κ' (gray circles). Different choices of $\hat{\kappa}$s have no significant effect on the eB dependence of Δ_s and Δ_p.

potential, nor in the definitions of $p_\parallel$ and $p_\perp$. In [52,62], however, whereas the Maxwell term is not included in the effective potential Ω_{eff}, it is included in the definitions (3.6) of anisotropic pressures.[18] To define a measure for the splitting of $p_\parallel$ and $p_\perp$ for nonvanishing eB, we define the splitting coefficient Δ_s for a fixed (T^*, μ^*) as [62]

$$\Delta_s(B;T^*,\mu^*) \equiv \left| \frac{p_\parallel(B;T^*,\mu^*) - p_\perp(B;T^*,\mu^*)|}{p(0;T^*,\mu^*)} \right|, \tag{3.8}$$

[18]Let us notice at this stage, that because of m independence of the Maxwell term, its presence or absence does not affect the values of constituent quark masses, that arise by minimizing Ω_{eff}. This is why we decided to remove the Maxwell term $-\frac{1}{4}F_{\mu\nu}F^{\mu\nu}$ from (2.1), and consequently $B^2/2$ from (2.2), (2.5) and (2.11). However, having in mind that this term has to be considered in the full thermodynamical potential, we have added it to $\Omega_{\text{eff}}^{\min}$ in the definitions of $p_\parallel$ and $p_\perp$ from (3.6).

where $p(0;T^*,\mu^*)$ is the pressure at fixed (T^*,μ^*) and for vanishing magnetic field. In Fig. 13(a), Δ_s is plotted as a function of eB at fixed temperature $T = 120$ MeV and for vanishing chemical potential. The results for κ_1, κ_2 and κ' are denoted by red squares, empty diamonds and gray circles, respectively. As it turns out, Δ_s increases with increasing magnetic field eB, as expected [62]. This specific feature is, in particular, not affected by different choices for $\hat{\kappa}$. Small deviations, up to maximum 0.4% occur only in the strong field regime, and increase with increasing eB. In comparison with $\hat{\kappa} = 0$ GeV^{-1}, the same maximum deviation occurs is in the strong-field regime, and as it turns out nonvanishing $\hat{\kappa}$ has a negative effect on Δ_s, especially in the strong-field regime. The same observation is also made in [11].

Another useful quantity that quantifies the relation between $p_\parallel$ and $p_\perp$ is Δ_p, [11]

$$\Delta_p(B;T^*,\mu^*) \equiv \left| \frac{p_\perp(B;T^*,\mu^*)}{p_\parallel(B;T^*,\mu^*)} \right|, \tag{3.9}$$

where (T^*,μ^*) are fixed temperature and chemical potential. As it turns out from Fig. 13(b), Δ_p has a minimum for a certain $eB_{\min} = 0.04$ GeV^2, and then increases and has a maximum for another $eB_{\max} = 0.08$ GeV^2. It then decreases to values $\Delta_p \sim 1$. Almost no differences occurs between different $\hat{\kappa}$s. Let us notice, that $eB_{\min}$ and $eB_{\max}$ are related to the specific magnetic fields, where $p_\perp$ and $p_\parallel$ almost vanish. As it turns out, $eB_{\min} \neq eB_{\max}$. This tiny difference is not visible in Fig. 12. The thermodynamical properties of $p_\perp/p_\parallel$, a quantity similar to Δ_p from (3.9), are considered in [11]. Here, the effect of AMM of neutrons and protons is studied on the bulk properties of a magnetized Fermi gas. It is shown that the AMM of protons and neutrons enhance the pressure anisotropy, that arises from the presence of constant background magnetic fields. As concerns the effect of the quark AMM on Δ_s and Δ_p, no such effect is observed in Fig. 13. In what follows, we will show that although both parallel and perpendicular pressures, as well as the pressure anisotropy remain (almost) unaffected by the inclusion of a large nonperturbative quark AMM, the magnetization of quark matter is strongly affected by it.

The pressure anisotropy has various effects on astrophysics of dense stellar objects [62,63] and the experiments of heavy ion collisions [32]. In [26,30,32], for instance, the magnetization of quark matter M is determined as a function of temperature. In [32] is shown that in the vicinity of the chiral transition point, the magnetization M is positive, and therefore hot and dense QCD at transition point exhibits a paramagnetic response. It is further shown, that the paramagnetic behavior of QCD matter affects the phenomenology of heavy ion collision, and in particular, has "significant impact on the value of elliptic flow v_2." In Fig. 14(a), the product of the magnetization M and the magnetic field strength B is plotted for our hot and dense

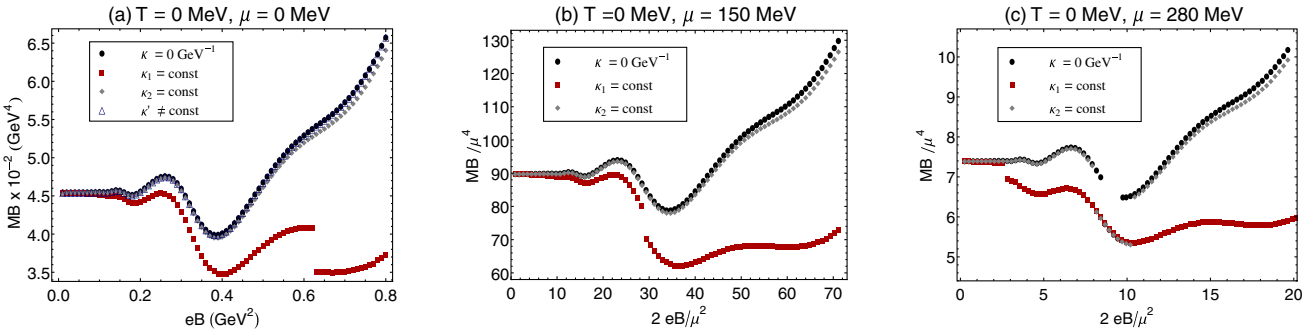

FIG. 14 (color online). (a) The product of the magnetization M and the magnetic field strength B of a two-flavor NJL model is plotted at $T = \mu = 0$ MeV, and for $\hat{\kappa} = 0$ GeV^{-1} (black circles), κ_1 (red squares), κ_2 (gray diamonds) and κ' (empty triangles). (b) and (c) The dimensionless quantity MB/μ^4 is plotted as a function of $2eB/\mu^2$ at $T = 0$ MeV, $\mu = 120$ MeV (panel b) and $\mu = 280$ MeV (panel c) as well as for $\hat{\kappa} = 0$ GeV^{-1} (black circles), κ_1 (red squares), and κ_2 (gray diamonds).

NJL model at $T = \mu = 0$ and for $\hat{\kappa} = 0$ GeV^{-1} (black circles), κ_1 (red squares), κ_2 (gray diamonds), and κ' (empty triangles). As it turns out, the results for κ_1 have significant difference with the results corresponding to $\hat{\kappa} = 0$ GeV^{-1}, κ_2 and κ'. As expected, at $T = 0$ MeV, there is no difference between the eB dependence of MB for $\hat{\kappa} = 0$ GeV^{-1} and κ'. The difference between the data for $\hat{\kappa} = 0$ GeV^{-1} and κ_2 becomes only significant in the LLL dominant regime $eB > 0.5$ GeV^2. In this regime, as expected, the dHvA oscillations arising in the regime $eB < 0.5$ GeV^2 weaken, and MB monotonically increases with increasing eB. These oscillations are also previously observed in [21,25]. The discontinuity arising in the data for κ_1 at $eB = 0.623$ GeV^2 (red squares), is related to the first-order phase transition from the χSB into the pχSR phase, demonstrated in Fig. 8. The latter leads also to a discontinuity in the eB dependence of the constituent quark mass exactly for $eB = 0.623$ GeV^2 [see Fig. 1(a)]. In Figs. 14(b) and (c), the dimensionless quantity MB/μ^4 is plotted as a function of $2eB/\mu^2$ at $T = 0$ MeV and $\mu = 150$ MeV [Fig. 14(b)] and $\mu = 280$ MeV [Fig. 14(c)] as well as different $\hat{\kappa}s$. Black circles, red squares and gray diamonds denote the results for $\hat{\kappa} = 0$ GeV^{-1}, κ_1 and κ_2, respectively. This dependence is also studied in [51] in the regime $2eB/\mu^2 \in [0, 1]$ for $\mu = 300$ MeV. Similar to the results of $\mu = 0$ MeV, the difference between $\hat{\kappa} = 0$ GeV^{-1} and κ_2 increases with increasing eB. Except in the regime of weak magnetic field $eB \lesssim 0.17$ GeV^2 ($2eB/\mu^2 \lesssim 15$ for $\mu = 150$ MeV), and $eB \lesssim 0.08$ GeV^2 ($2eB/\mu^2 \lesssim 2$ for $\mu = 280$ MeV), MB/μ^4 for κ_1 is smaller than the data for $\hat{\kappa} = 0$ GeV^{-1} and κ_2. According to the T-eB phase diagram for $\mu = 280$ MeV in Fig. 9, we expect discontinuities in the eB dependence of MB/μ^4 in the regime $0.34 < eB \leq 0.39$ GeV^2 ($8.7 \lesssim 2eB/\mu^2 \leq 10$) for $\hat{\kappa} = 0$ GeV^{-1}, $eB \simeq 0.155$ GeV^2 ($2eB/\mu^2 \sim 3.95$) for κ_1 and $0.3 < eB \leq 0.4$ GeV^2 ($7.7 < 2eB/\mu^2 \leq 10.2$) for κ_2. We conclude that discontinuities in the eB dependence of MB or MB/μ^4 as functions of eB are related, as expected, to first-order chiral phase transitions at certain magnetic fields and for fixed values of T and μ.

IV. CONCLUDING REMARKS

In recent years, there were a number of attempts to explore the effect of the quark AMM on the phase diagram of QCD at finite temperature, chemical potential and in the presence of uniform magnetic fields [11,50–52]. Following the method used in [11], we have studied, in the present paper, the effects of the (effective) quark AMM on the thermodynamic properties of the constituent quark mass m, and on the full phase portrait of a two-flavor magnetized NJL model at finite T and μ. The quark AMM is introduced via an additional minimal coupling term, $\hat{a}\sigma_{\mu\nu}F^{\mu\nu}$, in the Lagrangian density of the NJL model [54]. The coefficient $\hat{a}$, defined by $\hat{a} = \hat{Q}\,\hat{\alpha}\,\mu_B$, includes the nonperturbative (effective) Bohr magneton $\mu_B = \frac{e}{2m}$, and is herewith, a function of the constituent quark mass, and receives (T, μ, eB) corrections. As it turns out, $\hat{a}\sigma_{\mu\nu}F^{\mu\nu}$ leads to an additional term proportional to $T_f = \kappa_f q_f eB$ in the quark energy dispersion relation (2.9). In the above expression, $f = u, d$ stands for up (u) and down (d) quark flavors, and the dimensionful coupling κ_f is defined by $\kappa_f = \frac{\alpha_f}{2m}$, with α_f related to the deviation of the Landé g factor from 2. Our aim was, in particular, to study the effects of constant as well as T-, μ-, and eB-dependent effective coupling κ_f on the thermodynamic behavior of m, as well as on the phase portrait of the hot, dense and magnetized quark matter, described by our model. To this purpose, three different sets for the effective coupling κ_f are chosen. To do this, we used the method presented in Sec. II and Appendix [see (2.12)–(2.14)]. The dependence of the constituent quark mass m on T, μ, and eB was then determined for each fixed κ_f in Sec. III A (see Figs. 1–7). Here, we have explicitly described the signatures related to the phenomena of MC and IMC. We have further shown that for large enough κ_f, even in the regime of strong magnetic fields, the eB dependence of m is strongly affected by the phenomenon of IMC. Then, using the one-loop effective potential Ω_{eff} from (2.11) in terms of κ_f, we have explored

the complete phase portrait of the model in the parameter space T, μ, eB, and κ_f (see Sec. III B). We have shown, that for large enough κ_f and mainly in the regime of weak magnetic fields $eB < 0.5$ GeV^2, the critical temperature T_c and critical chemical potential μ_c decrease with increasing eB. This is related to the phenomenon of IMC. Moreover, it is shown that in certain regimes of the parameter space, the phenomenon of reentrance of chiral symmetry broken phase occurs, mainly as a consequence of dHvA oscillations [23]. Also, the order of the phase transition turns out to be affected by κ_f (see Figs. 8–11). In Sec. III C, the pressure anisotropy of the quark matter in the longitudinal and transverse directions with respect to the magnetic field is considered. We have shown that different choices of κ_f have any significant effect on the pressure anisotropies, demonstrated in Fig. 12, and on Δ_s and Δ_p, as quantitative measures for these anisotropies (see Fig. 13). In Fig. 14, the eB dependence of the product of the field strength and the magnetization is demonstrated. We have shown that for large enough κ_f, this product becomes smaller than for the cases of $\hat{\kappa} = 0$ GeV^{-1} and small κ_f, but the magnetization is always positive. According to [32], this is believed to be an indication of paramagnetic behavior of the hot and magnetized quark matter, especially in the vicinity of the phase transition point.

To what extent the inclusion of large nonperturbative quark AMM in more sophisticated models, such as magnetized Polyakov-loop NJL (PNJL) model or Polyakov-loop linear-sigma (PLSM) model, would affect the critical temperature and the order of confinement/deconfinement phase transition is an open question, which shall be investigated in the future; one of the interesting phenomena that occurs by considering a new order parameter corresponding to the confinement/deconfinement phase transition (Polyakov loop) is the appearance of a new phase in the T-eB phase diagram of magnetized Polyakov-loop extended effective models, where the deconfined quark matter is in the χSB phase. As is shown, e.g., in [64], the main reason for the appearance of this new phase in a magnetized PLSM model is the eB dependence of the critical temperature corresponding to χSB, $T_c^{\chi\mathrm{SB}}$, and the critical temperature corresponding to confinement/deconfinement phase transition, T_c^{conf}. In this model, for vanishing quark AMM, $T_c^{\chi\mathrm{SB}}(B)$ increases with increasing eB, while $T_c^{\mathrm{conf}}(B)$ decreases. This opens a possibility for the appearance of the aforementioned new deconfined but χSB phase. For vanishing quark AMM, the phenomenon of IMC, observed in lattice QCD simulations changes this picture in the sense that if both $T_c^{\chi\mathrm{SB}}(B)$ and $T_c^{\mathrm{conf}}(B)$ decreases with increasing eB, the region in the T-eB phase space, where the new phase may exist, shrinks. To answer to the question whether this new phase survives the inclusion of large nonperturbative quark AMM in a magnetized Polyakov-loop extended effective model, it is crucial to determine the behavior of T_c^{conf} as a function of eB in these kind of models including the quark AMM. Other extensions to the model considered in the present paper are also thinkable. As it is shown in [65] the inclusion of β equilibrium and isospin asymmetry in a magnetized NJL model affect the order of the phase transition, and consequently shift the position of the critical point in a T-μ phase diagram. Similarly, according to [66], the addition of a strong enough vector interaction to the magnetized NJL Lagrangian strongly affects the order of phase transitions, the softness of the equation of state and the position of the critical point in a T-μ phase diagram (vector repulsion). All these would have, for instance, astrophysical implications, would affect the structure of compact stellar objects [66], and might also be interesting for the physics of HICs. It would be interesting to study the interplay between the effects occurring by considering large nonperturbative quark AMMs and the effects induced by the presence of the above listed extensions to magnetized NJL-like models, including isospin-asymmetry, different inhomogeneities, β equilibrium, strangeness and additional vector channels in the NJL-like models. We postpone these interesting studies to future publications.

Let us notice at this stage, that the method used in the present paper to introduce the quark AMM is different from the method presented in [50]. Here, starting from a one-flavor magnetized NJL model with an appropriate tensor channel, a mechanism for the dynamical generation of the quark AMM in the LLL is presented. It is also shown that the scalar and tensor couplings of the NJL model become anisotropic, and receive longitudinal and transverse components with respect to the direction of the magnetic field. For constant anisotropic couplings, in the subcritical regime, the phenomenon of IMC does not occur. In a subsequent paper [48], however, the authors consider the running of these couplings as a function of eB, and show that because of a certain antiscreening effect, induced by quarks that are confined by the magnetic fields to the LLL, the critical temperature of the χSB decreases with increasing the magnetic field strength. This is believed to be a natural explanation for the phenomenon of IMC, that arises originally in a number of model calculations [17,22], in the framework of gauge/gravity duality [16], and from an ab initio lattice QCD simulation at finite T and eB [28].

Let us also notice that the linear-in-B ansatz, used in the present paper, is different from the one which is used in [51,52]. Here, the Schwinger term is defined to be proportional to the Bohr magneton $\mu_B^0 = \frac{e}{2m_0}$ in terms of the current (bare) quark mass m_0, in contrast to our approach, described above. Thus far, the inconsistencies from the Schwinger linear-in-B ansatz in the weak-magnetic field approximation, described in [51,52], are not expected to occur in our approach. Moreover, in contrast to the previous approaches, we have considered the contributions of all Landau levels, and neither restricted ourselves to LLL [50], nor to one-loop approximation in the LLL, as in [51,52].

Apart from the aforementioned extensions. there are many possibilities to improve the approach presented in this paper. As we have argued in Sec. II, the coefficient κ_f and the constituent quark mass m are closely entangled. In other words, it is not possible to determine one of them without determining the other one. The reason is indeed formulated in [50], where it is stated that since one and the same symmetry is broken by the quark AMM and the chiral condensate, nothing can guarantee a vanishing AMM, once the chiral symmetry is broken by a nonvanishing chiral condensate. In the present paper, using a method compatible with the constituent quark model, we have fixed κ_f and determined m. This method can gradually be improved. The main idea is to determine κ_f from the relation $\kappa_f = \frac{1}{2m}(\frac{m}{I_f} - 1)$, where I_f for up and down quarks are given in (A8). Instead of fixing m with the phenomenologically reliable $M = 420$ and $M = 340$ MeV, as it is performed in the present paper, we can replace it, e.g., by $m_0(T) \equiv m(T, \mu^*, eB^*; \hat{\kappa} = 0)$, where μ^* and eB^* are fixed values of chemical potential and magnetic field. We then obtain

$$\kappa_u(T, \mu^*, eB^*) = \frac{1}{2m_0(T)}\left(\frac{m_0(T)}{0.338} - 1\right),$$

for up quarks, and

$$\kappa_d(T, \mu^*, eB^*) = \frac{1}{2m_0(T)}\left(\frac{m_0(T)}{0.322} - 1\right),$$

for down quarks. Plugging these relations into (2.9), and the latter into $\Omega_{\text{eff}}(m_0(T); T, \mu^*, eB^*)$, and eventually looking for the global minima of the resulting expression, a new set of constituent quark mass arises, which replaces the data demonstrated in Fig. 6, for instance. The same procedure may be repeated for the sets (T^*, μ, eB^*) or (T^*, μ^*, eB), where the fixed values of T, μ, and eB are denoted by the superscript "star." It would be interesting to look for the phenomenon of MC and IMC in this framework. We will report about the results of this new approach in the a future publication.

ACKNOWLEDGMENTS

The authors acknowledge F. Ardalan for discussions about the effect of the anomalous magnetic moment of quarks on their spectra, M. R. Ejtehadi for bringing the importance of the reentrance phenomenon in condensed matter physics to our attention, and M. Mohammadi Najafabadi for providing insight into the experimental data for the magnetic moment of protons and neutrons. We thank also the referee of the present paper for suggestions concerning extending our model in order to study the interplay between various effects of these extensions with the effects observed in the present paper.

APPENDIX: DETERMINATION OF $\hat{\kappa}$ USING THE CONSTITUENT QUARK MODEL

Let us consider a system including up and down quarks in the presence of a uniform magnetic field $\mathbf{B}$. The spin magnetic moment $\hat{\boldsymbol{\mu}}$ of this system is given by

$$\hat{\boldsymbol{\mu}} = g\hat{Q}\hat{\mu}_B\mathbf{s}. \tag{A1}$$

Here, $g = 2(1 + \hat{\alpha})$ is the Landé g-factor, with $\hat{\alpha}$ denoting its anomalous contribution. In our two-flavor NJL model $\hat{\alpha} = \text{diag}(\alpha_u, \alpha_d)$ and $\hat{Q} = \text{diag}(q_u, q_d)$ are 2×2 diagonal matrices, including the anomalous magnetic moment $\alpha_f, f = u, d$ and electric charge $q_f, f = u, d$ of the up and down quarks. Moreover, $\mathbf{s} = \frac{1}{2}\boldsymbol{\tau}$ is the quark spin angular momentum of the quarks, and $\hat{\mu}_B = \text{diag}(\mu_B^u, \mu_B^d)$ with $\mu_B^f = \frac{e}{2M_f}, f = u, d$, the nonperturbative (effective) Bohr magneton in the flavor space, which is given in terms of the (bare) electric charge e, as well as the up and down quark constituent (effective) masses M_u and M_d, arising in the mass matrix $\hat{M} = \text{diag}(M_u, M_d)$. Here, $\boldsymbol{\tau}$ are the three Pauli matrices. Using (A1), and assuming that the magnetic field $\mathbf{B}$ is directed in the third direction, the fth matrix element of the third component of $\hat{\boldsymbol{\mu}}$, $\hat{\mu}_3 = \text{diag}(\mu_u, \mu_d)$, is given by

$$\mu_f = \frac{q_f e}{2M_f}(1 + \alpha_f)\sigma_3. \tag{A2}$$

Here, $\sigma_3 = \text{diag}(+1, -1)$ is the third Pauli matrix. The eigenvalues of μ_f in the spinor space are therefore given by $\mu_f = \frac{q_f e}{2M_f}(1 + \alpha_f)s$ with $s = \pm 1$ and $f = u, d$. Using this expression, we can define the following positive ratio

$$I_f \equiv \frac{M_f}{1 + \alpha_f} = \frac{\mu_N}{\mu_f} q_f m_p, \tag{A3}$$

which turns out to be a phenomenologically relevant quantity [56]. Here, $m_p \sim 0.938$ GeV the proton mass, and $\mu_N \equiv \frac{e}{2m_p}$ the nuclear magneton, whose phenomenological values are fixed by experiments. Using at this stage,

$$\mu_p \sim 2.79\mu_N, \qquad \mu_n \sim -1.91\mu_N, \tag{A4}$$

for the magnetic moment of proton (neutron) μ_p (μ_n), and their relationship to the magnetic moment of up and down quarks, μ_u and μ_d,

$$\mu_p = \frac{1}{3}(4\mu_u - \mu_d), \qquad \mu_n = \frac{1}{3}(4\mu_d - \mu_u), \tag{A5}$$

that yield

$$\mu_u = \frac{1}{5}(4\mu_p + \mu_n), \qquad \mu_d = \frac{1}{5}(4\mu_n + \mu_p), \tag{A6}$$

we obtain

$$\mu_u \sim 1.852\mu_N, \qquad \mu_d \sim -0.972\mu_N. \tag{A7}$$

Using these data, the ratio $I_f = \frac{\mu_N}{\mu_f} q_f m_p$ for $f = u, d$ is fixed to be

$$I_u \sim 0.338 \text{ GeV}, \qquad I_d \sim 0.322 \text{ GeV}. \tag{A8}$$

Same results are also reported in [56]. The above phenomenological values for $I_f, f = u, d$ can be used to determine phenomenological values for $\alpha_f, f = u, d$ through $I_f = \frac{M_f}{1+\alpha_f}$ from (A3). In order to have a sizable quark AMM, we choose $M_u = M_d = 0.420$ GeV for the quark (effective) constituent mass $M_f, f = u, d$ [56]. We arrive at

$$\alpha_u \sim 0.242, \qquad \alpha_d \sim 0.304, \tag{A9}$$

which satisfy the condition $\alpha_u - \alpha_d \simeq 0.05$. The latter guarantees the isospin symmetry [56]. Plugging (A9) into the relation $\kappa_f = \frac{\alpha_f}{2M_f}$ from (2.9), and choosing $M_u = M_d = 0.420$ GeV, we obtain

$$\kappa_u \sim 0.290, \qquad \kappa_d \sim 0.360 \text{ GeV}^{-1}, \tag{A10}$$

[see also (2.12)]. Choosing, on the other hand, $M_u = M_d = 0.340$ GeV, and following the same steps as above, we obtain

$$\alpha_u \sim 0.006, \qquad \alpha_d \sim 0.056, \tag{A11}$$

which lead to

$$\kappa_u \sim 0.009, \qquad \kappa_d \sim 0.080 \text{ GeV}^{-1}, \tag{A12}$$

[see also (2.13)]. As described in Sec. II, in the present work, $\hat{\kappa}$, appearing explicitly in the quark energy dispersion relation (2.9) is fixed by (A10) and (A12) [see (2.12) and (2.13)]. The T-, μ-, and eB-dependent constituent quark mass are then determined by plugging this dispersion relation into the thermodynamic potential (2.11), and minimizing it appropriately. We have shown that for $\hat{\kappa}_1$ from (A10), leading to large $\hat{\alpha}$ from (A9), the phenomenon of IMC occurs.

[1] D. E. Kharzeev, K. Landsteiner, A. Schmitt, and H. U. Yee, Lect. Notes Phys. **871**, 1 (2013).
[2] V. de la Incera, AIP Conf. Proc. **1361**, 74 (2011).
[3] R. C. Duncan and C. Thompson, Astrophys. J. **392**, L9 (1992).
[4] V. Skokov, A. Y. Illarionov, and V. Toneev, Int. J. Mod. Phys. A **24**, 5925 (2009).
[5] D. E. Kharzeev, L. D. McLerran, and H. J. Warringa, Nucl. Phys. **A803**, 227 (2008).
[6] K. Tuchin, Adv. High Energy Phys. **2013**, 490495 (2013).
[7] U. Gursoy, D. Kharzeev, and K. Rajagopal, Phys. Rev. C **89**, 054905 (2014).
[8] S. Fayazbakhsh, S. Sadeghian, and N. Sadooghi, Phys. Rev. D **86**, 085042 (2012).
[9] S. Fayazbakhsh and N. Sadooghi, Phys. Rev. D **88**, 065030 (2013).
[10] J. O. Andersen, Phys. Rev. D **86**, 025020 (2012); J. High Energy Phys. 10 (2012) 005.
[11] M. Strickland, V. Dexheimer, and D. P. Menezes, Phys. Rev. D **86**, 125032 (2012).
[12] G. S. Bali, F. Bruckmann, G. Endrodi, and A. Schäfer, Phys. Rev. Lett. **112**, 042301 (2014).
[13] K. G. Klimenko, Z. Phys. C **54**, 323 (1992).
[14] V. P. Gusynin, V. A. Miransky, and I. A. Shovkovy, Nucl. Phys. **B462**, 249 (1996).
[15] I. A. Shovkovy, Lect. Notes Phys. **871**, 13 (2013).
[16] F. Preis, A. Rebhan, and A. Schmitt, J. High Energy Phys. 03 (2011) 033.
[17] T. Inagaki, D. Kimura, and T. Murata, Prog. Theor. Phys. **111**, 371 (2004).
[18] V. Zdravkov, A. Sidorenko, G. Obermeier, S. Gsell, M. Schreck, C. Müller, S. Horn, R. Tidecks, and L. Tagirov, Phys. Rev. Lett. **97**, 057004 (2006).
[19] A. N. Berker and J. S. Walker, Phys. Rev. Lett. **47**, 1469 (1981).
[20] J. Margueron and E. Khan, Phys. Rev. C **86**, 065801 (2012).
[21] S. Fayazbakhsh and N. Sadooghi, Phys. Rev. D **82**, 045010 (2010).
[22] S. Fayazbakhsh and N. Sadooghi, Phys. Rev. D **83**, 025026 (2011).
[23] W. J. de Haas and P. M. van Alphen, Proc. Acad. Sci. (Amsterdam) **33**, 1106 (1930); L D. Landau and E. M. Lifshitz, *Statistical Physics* (Pergamon Press, New York, 1980).
[24] D. Ebert and A. S. Vshivtsev, arXiv:hep-ph/9806421; T. Inagaki, D. Kimura, and T. Murata, Prog. Theor. Phys. Suppl. **153**, 321 (2004).
[25] J. L. Noronha and I. A. Shovkovy, Phys. Rev. D **76**, 105030 (2007); **86**, 049901(E) (2012); K. Fukushima and H. J. Warringa, Phys. Rev. Lett. **100**, 032007 (2008).
[26] V. D. Orlovsky and Y. A. Simonov, arXiv:1406.1056.
[27] P. V. Buividovich, M. N. Chernodub, E. V. Luschevskaya, and M. I. Polikarpov, Phys. Lett. B **682**, 484 (2010);

P. V. Buividovich, M. I. Polikarpov, and O. V. Teryaev, Lect. Notes Phys. **871**, 377 (2013).
[28] G. S. Bali, F. Bruckmann, G. Endrodi, Z. Fodor, S. D. Katz, S. Krieg, A. Schäfer, and K. K. Szabo, J. High Energy Phys. 02 (2012) 044; G. S. Bali, F. Bruckmann, G. Endrodi, Z. Fodor, S. D. Katz, and A. Schäfer, Phys. Rev. D **86**, 071502 (2012); G. S. Bali, F. Bruckmann, M. Constantinou, M. Costa, G. Endrdi, Z. Fodor, S. D. Katz, S. Krieg, H. Panagopoulos, and A. Schäfer, *Proc. Sci.*, ConfinementX2012 (2012) 197.
[29] E.-M. Ilgenfritz, M. Muller-Preussker, B. Petersson, and A. Schreiber, Phys. Rev. D **89**, 054512 (2014); V. G. Bornyakov, P. V. Buividovich, N. Cundy, O. A. Kochetkov, and A. Schäfer, Phys. Rev. D **90**, 034501 (2014).
[30] C. Bonati, M. D'Elia, M. Mariti, F. Negro, and F. Sanfilippo, Phys. Rev. D **89**, 054506 (2014).
[31] F. Bruckmann, G. Endrodi, and T. G. Kovacs, J. High Energy Phys. 04 (2013) 112.
[32] G. S. Bali, F. Bruckmann, G. Endrodi, S. D. Katz, and A. Schäfer, J. High Energy Phys. 08 (2014) 177.
[33] K. Fukushima and J. M. Pawlowski, Phys. Rev. D **86**, 076013 (2012).
[34] J. O. Andersen, W. R. Naylor, and A. Tranberg, J. High Energy Phys. 04 (2014) 187.
[35] K. Kamikado and T. Kanazawa, J. High Energy Phys. 03 (2014) 009.
[36] K. Fukushima and Y. Hidaka, Phys. Rev. Lett. **110**, 031601 (2013).
[37] R. L. S. Farias, K. P. Gomes, G. I. Krein, and M. B. Pinto, Phys. Rev. C **90**, 025203 (2014).
[38] A. J. Mizher, M. N. Chernodub, and E. S. Fraga, Phys. Rev. D **82**, 105016 (2010).
[39] R. Gatto and M. Ruggieri, Phys. Rev. D **83**, 034016 (2011).
[40] M. Ferreira, P. Costa, D. P. Menezes, C. Providência, and N. Scoccola, Phys. Rev. D **89**, 016002 (2014); **89**, 019902(E) (2014).
[41] M. Ferreira, P. Costa, O. Loureno, T. Frederico, and C. Providência, Phys. Rev. D **89**, 116011 (2014).
[42] E. S. Fraga, B. W. Mintz, and J. Schaffner-Bielich, Phys. Lett. B **731**, 154 (2014).
[43] J. O. Andersen, W. R. Naylor, and A. Tranberg, J. High Energy Phys. 04 (2014) 187.
[44] R. Gatto and M. Ruggieri, Phys. Rev. D **85**, 054013 (2012).
[45] J. Chao, P. Chu, and M. Huang, Phys. Rev. D **88**, 054009 (2013); L. Yu, H. Liu, and M. Huang, Phys. Rev. D **90**, 074009 (2014).
[46] M. Ruggieri, L. Oliva, P. Castorina, R. Gatto, and V. Greco, arXiv:1402.0737.
[47] A. Ayala, M. Loewe, A. J. Mizher, and R. Zamora, Phys. Rev. D **90**, 036001 (2014); A. Ayala, M. Loewe, and R. Zamora, arXiv:1406.7408.
[48] E. J. Ferrer, V. de la Incera, and X. J. Wen, arXiv:1407.3503.
[49] J. P. Blaizot, E. S. Fraga, and L. F. Palhares, Phys. Lett. B **722**, 167 (2013).
[50] E. J. Ferrer, V. de la Incera, I. Portillo, and M. Quiroz, Phys. Rev. D **89**, 085034 (2014).
[51] E. J. Ferrer, de la Incera, D. M. Paret, and A. P. Martnez, in *Proceedings of the Compact Stars in the QCD Phase Diagram III (CSQCD III), 2012*, Guarujá, Brazil, http://www.astro.iag.usp.br/foton/CSQCD3.
[52] D. M. Paret, A. P. Martinez, E. J. Ferrer, and V. de la Incera, in *Proceedings of the STARS2013 2nd Caribbean Symposium on Cosmology, Gravitation, Nuclear and Astroparticle Physics/SMFNS 3rd International Symposium on Strong Electromagnetic Fields and Neutron, 2013*, Havana/Varadero, Cuba.
[53] E. J. Ferrer and V. de la Incera, Nucl. Phys. **B824**, 217 (2010); Phys. Rev. Lett. **102**, 050402 (2009); B. Feng, E. J. Ferrer, and V. de la Incera, Nucl. Phys. **B853**, 213 (2011).
[54] J. S. Schwinger, Phys. Rev. **73**, 416 (1948).
[55] B. L. Ioffe and A. V. Smilga, Nucl. Phys. **B232**, 109 (1984).
[56] P. J. A. Bicudo, J. E. F. T. Ribeiro, and R. Fernandes, Phys. Rev. C **59**, 1107 (1999).
[57] G. Peressutti and B. S. Skagerstam, Phys. Lett. **110B**, 406 (1982); J. Shen, H.-H. Xu, and C.-H. Tsai, Commun. Theor. Phys. **15**, 209 (1991).
[58] S. S. Masood and M. Q. Haseeb, Int. J. Mod. Phys. A **27**, 1250188 (2012).
[59] V. I. Ritus, Ann. Phys. (N.Y.) **69**, 555 (1972).
[60] G. Murguia, A. Raya, A. Sanchez, and E. Reyes, Am. J. Phys. **78**, 700 (2010); N. Sadooghi and F. Taghinavaz, Phys. Rev. D **85**, 125035 (2012).
[61] D. Ebert and V. C. Zhukovsky, Mod. Phys. Lett. A **12**, 2567 (1997); V. P. Gusynin and I. A. Shovkovy, Phys. Rev. D **56**, 5251 (1997); D. Ebert, K. G. Klimenko, H. Toki, and V. C. Zhukovsky, Prog. Theor. Phys. **106**, 835 (2001).
[62] D. M. Paret, J. E. Horvath, and A. P. Martinez, arXiv:1407.2280.
[63] M. Chaichian, S. S. Masood, C. Montonen, A. Perez Martinez, and H. Perez Rojas, Phys. Rev. Lett. **84**, 5261 (2000).
[64] A. J. Mizher, M. N. Chernodub, and E. S. Fraga, Phys. Rev. D **82**, 105016 (2010).
[65] P. Costa, M. Ferreira, H. Hansen, D. P. Menezes, and C. Providência, Phys. Rev. D **89**, 056013 (2014).
[66] D. P. Menezes, M. B. Pinto, L. B. Castro, P. Costa, and C. Providência, Phys. Rev. C **89**, 055207 (2014).